Dipartimento di Scienze Matematiche "Giuseppe Luigi Lagrange"
Corso di Laurea in Ingegneria Matematica, Indirizzo Modelli Matematici e Simulazioni Numeriche
TESI DI LAUREA MAGISTRALE

REDUCED ORDER METHODS FOR HEMODYNAMICS MODELLING

ADVISORS:
Prof. Claudio Canuto
Prof. Gianluigi Rozza
CO-ADVISOR:
Dr. Francesco Ballarin
Dr. Michele Girfoglio

CANDIDATE
Giuseppe Infantino

Academic year 2019/2020

Ai miei genitori,
ringraziandoli per i loro sacrifici.

Alla professoressa Lilli.

Abstract

Left ventricular assist devices (LVADs) are used to provide haemodynamic support to patients with critical cardiac failure. Severe complications can occur because of the modifications of the blood flow in the aortic region. In this work, the effect of a continuous flow LVAD device on the aortic flow is investigated by means of a non-intrusive reduced order model (ROM) built using the proper orthogonal decomposition with interpolation (PODI) method. The full order model (FOM) is represented by the incompressible Navier-Stokes equations discretized by using Finite Volume (FV) and Finite Element (FE) techniques, coupled with three-element Windkessel models to enforce outlet boundary conditions in a multi-scale approach. A patient-specific framework is proposed: a personalized geometry reconstructed from Computed Tomography (CT) images is used and the individualisation of the coefficients of the three-element Windkessel models is based on experimental data provided by the Right Heart Catheterization (RCH) and Echocardiography (ECHO) tests. Pre-surgery configuration is also considered at FOM level in order to further validate the model. A parametric study with respect to the LVAD flow rate is considered. The accuracy of the reduced order model is assessed against results obtained with the full order model. We can split the reduced order model (ROM) methods in two stages: the first one, named *offline phase*, is the most expensive one it is the phase in which the so called full order solutions (or snapshots) are computed. Afterwards, in the *online phase*, the solution of the discrete problem is sought in a low-dimensional space in which all the mathemat objects as matrices and vectors are simply assembled with the objects computed in the offline phase and, for this reason, the computation is much faster.

The idea behind this project is to try to shift, thanks to proper algorithms, the computing power of a supercomputer on tablets and laptops with important national and international collaborations between mathematics, engineering and medicine.

If a surgeon could have a supercomputer available in the operating room, then the reading of a patient's "vascular geometry" could be absolutely immediate, however this is not the case today.

The basis of the work consists in creating computer simulations of mathematical models, i.e. reconstructing the portion of the cardiovascular system

under examination with a digital computer model. However, sometimes, these simulations can prove to be very expensive in terms of computational resources and what this project focuses on is to develop reduced-order numerical methods that serve to combine what is calculated with the supercomputer (offline phase), with calculations that, on the other hand, can be performed on a laptop or even on a tablet or mobile phone (online phase).

Contents

Acknowledgments

This thesis has been developed and created in collaboration with the MathLab group of SISSA (Trieste, Italy), whose members consistently follow and helped me to get and implement the numerical methods and results that the reader could finds in this work. First of all I want to say thank you to my thesis advisor prof. Claudio Canuto of Politecnico di Torino for giving me the opportunity to work on this project. A very special thank you goes also to prof. Gianluigi Rozza of Scuola Internazionale Superiore di Studi Avanzati (SISSA) for his kindness, professionalism, availability and for infinite helpfulness he made available during the beautiful period I spent in SISSA. A huge thank you goes also to Drs. Michele Girfoglio and Francesco Ballarin of SISSA, first of all for their professionalism and in addition for their availability, kindness, patience in listening and solving my doubts and problems. A huge thank you goes also to *Azienda Ospedaliera San Camillo, Unità Operativa Complessa di Cardiochirurgia e Chirurgia dei Trapianti, Roma* for collaborating by providing clinical data and CT scans of the patients analyzed in this thesis. We acknowledge the support provided by the European Research Council Executive Agency by the Consolidator Grant project AROMA-CFD "Advanced Reduced Order Methods with Applications in Computational Fluid Dynamics" - GA 681447, H2020-ERC CoG 2015 AROMA-CFD and INdAM-GNCS 2020 project "Tecniche Numeriche Avanzate per Applicazioni Industriali".

Giuseppe Infantino.

List of Figures

List of Tables

Introduction

Nowadays, cardiovascular diseases are, unfortunately, the main cause of death in developed countries. Heart failure is a globally increasing health problem, in fact, as emerges from a recent survey by the *World Health Organization* this kind of disease taking an estimated 17.9 million lives each year ([48]).

The goal of this thesis is to investigate the phenomena that characterize the Aorta (largest artery in the human body) during the cardiac cycle, in particular we will study the instant of the pumping of blood by the left ventricle, through the aortic valve, into the aorta; we will analyze the effects of introducing a LVAD (Left Ventricular Assist Device), the state-of-the-art technology that has the task of supporting the left ventricle (as the name of the technology suggests) and in case of severe ventricular failure even take its place if the ventricle presents functional issues during the cardiac cycle.

A ventricular assist device (VAD) consists of a mechanical pump which, in situations where one of the heart's natural pumps (in our case the left ventricle) does not work properly, it is activated to increase the quantity and therefore the flow of blood through the body.

Nowadays LVAD technology is the most viable alternative to heart transplants in case of malfunction of the heart, however it remains a high risk procedure because it is very invasive and it is severely affecting patient's daily life (for more details see [50]), although the implant still allows the person with advanced heart failure to be able to return to a more normal life than before.

The contribution that this thesis intends to provide to this area of research consists in reproducing the Aorta of some patients for whom TAC made in the hospital, are available, and to reconstruct the aorta as a computational domain, on which performing computational simulations that can provide results to be pontentially used by medicals treating patients in hospital. Considering the fact that the computational domain is actually a subset of a much larger real domain, a fundamental role for the accuracy of the computational setting is played by the boundary conditions, which we will explain and analyze in more detail below. However, as stated [3] and [4] the effect of boundary conditions on the CFD solution are very important and so they need to be defined carefully: in this work we propose a typical way of setting the boundary conditions in a hemodynamic problem: *lumped parameter (LP) representations of a part of the cardio-vascular system and an external excitation of the system with a blood pump*, as specified in [5].

Subsequently, the results obtained will be analyzed and discussed during the post-processing phase.

The structure of this work could be summarized as follows:

- at first, a description of VAD technology and cardiac cycle is illustrated and it is provided a short presentation of how this technology fits in the dynamics of the cardiac cycle. At this point it is descripted the mathematical model adopted: firstly we will present the continuous model (Navier-Stokes equations adapted to the specific problem), secondly the discretization techniques: as regards space discretization we will analyze Finite Element Method (FEM) with backflow stabilization and Finite Volume Method (FVM); as regards, instead, temporal discretization we will adopt Backward Differentiation Formula of order 1 (BDF1), see [32].

- After that we will consider a first familiarization with the work software and with the various aspects of the problem under consideration: in order to accomplish this, we will consider an healthy case, i.e., in this part, we will study the cardiac-cycle of an healthy person and we will select the physical variables of interest. Our first analysis consists in describing boundary conditions and initial conditions and analyzing some fluid dynamic quantities of interest related to this type of case, as for example: inlet velocity of the fluid (the blood) from the aortic valve (which will be the only inlet of the model), wall shear stress along the entire aortic surface, pressure along the entire aortic volume; we will obtain and collect results on the healthy person case through FOM simulations with both FEM and FVM approach. We will ascertain that the two methods provide very similar results and then we will proceed in our analysis following the latter. Once the framework is clear, the mathematical model will be validated testing the sick person pre-surgery and post-surgery cases comparing the results obtained with experimental results.

- Once the model is validated, we will introduce the reader to ROMs, providing some motivations and some basic concepts about theory and applications. We will present the methodologies that we will use in this thesis, i.e, Proper Orthogonal Decomposition (POD), with the Proper Orthogonal Decomposition with Interpolation (PODI) variant. At this point we will present the numerical results obtained, in the case of the sick person case, which is the case of application interest, with the ROM method and the results will be compared with those obtained with the FOM method.

The reasons why we analyze the problem using these techniques, which are synthetically called ROMs, is because one of the goals of this area of research is reducing the complexity of a mathematical model and its numerical approximation. Reduced order methods represents a wide class of techniques developed from different communities of research. The main scientifical field in which ROMs are applied is parametric Partial Differential Equations (PDEs): a parametric PDE is a PDE ([2]) in whose expression there are one or more parameters that we could vary, for example, to take into account the uncertainty or different operating conditions. Sometimes calculating and solving problems associated with parametric PDEs for particular parameter values it can be too expensive, especially for industrial applications, moreover it may be helpful to have the solution available for many parameter values; all this could lead to unmanageable computational times, for this reason and in these situations the ROMs become very useful or even, in some occasions, indispensable. The idea behind a reduced order model is to get a solution in much less time, however, it will be an approximate solution with respect to the solution that would have been obtained with a FOM applied to the same problem. In the effort of having a ROM solution that reproduces as accurately as possible the FOM one, a whole area of this research area is dedicated to the analysis of the error between the ROM solution and the FOM solution, but we will not analyze this aspect in this work.

In this work, we will consider just one parameter: the *flow rate* of the pump.

In order to obtain a model able to re-produce clinical configurations, geometry is reconstructed from patient-specific Computed Tomography (CT) images. Moreover, a multi-scale approach was adopted by coupling three-element Windkessel models [52], used as boundary conditions and whose parameters are estimated by using experimental data provided by Right Heart Catheterization (RHC) and Echocardiography (ECHO) tests, with the Aorta model.

This work has been carried out in the framework of an intership at SISSA, International School for Advanced Studies, Mathematics Area, mathlab laboratory, within ERC-AROMA-CFD project: the framework developed within AROMA-CFD will provide attractive capabilities for several industrial and medical applications (e.g. aeronautical, mechanical, naval, biomedical engineering and cardiovascular surgery as well), combining high performance computing (in dedicated supercomputing centers) and advanced reduced order modelling (in common devices), to guarantee real time computing and visualization.

Trieste and Torino, July 2020

Chapter 1

Cardiovascular system and VAD

Left ventricular assist devices (LVADs) are needed by patients with circulatory issues in the left ventricle of the heart. They are currently used in a wide range of diseases as post-infarction heart failure. Lots of works treat about the numerical and computational investigation of the hemodynamics in the aortic region in the presence of a LVAD device, both in a single configuration [80] and varying of some physical (LVAD flow rate [36], [37]) and geometrical (cannula angle [74, 33, 70, 71, 38] and anastomosis position [39, 73, 72, 79, 33, 70, 37, 75, 81, 40, 36. 41]) parameters. As said before, in this work we will consider just one parameter: *the flow rate* of the pump.

1.1 Anatomy of the cardiovascular system

In this section we will briefly analyze the structure of the heart, in particular for the purpores of this thesis we will focus in the left ventricle. We will also analyze the cardiac cycle, explaining how it can change once LVAD is surgically transplanted into the patient.

1.1.1 Brief description of the heart

The hearth is a muscular organ made of two synchronised pumps in parallel: the right side that both perfuses the lungs and receives deoxygenated blood carried by the systemic veins and the left side which, instead, collects oxygenated blood from the pulmonary veins and perfuses the rest of the body ([6]).

The heart has four cavities: left atrium and right atrium that collect the blood from the veins, left ventricle and right ventricle that pump the blood into the systemic and polmunary veins. For the purposes of this work we will focus on the left ventricle: it is the largest chamber with the thicket walls and it is located behind and leftwards from the right ventricle.

The two ventricles share a septum, which separates the heart into left and right sides. There are four valves in the hearth, one at the exit of each hearth cavity, the one that we are interested in for our work is the aortic valve through which the left ventricle ejects blood into the aorta. The aortic valve has three simple leaflets that come together without any attachments, providing in this way mutual support when they are closed, for more details see [6].

1.1.2 The cardiac cycle

The cardiac cycle is what happens in the human heart during a heartbeat, it consists in a two stage pumping action over a period of about 1 s. These two stages are: systole that consists in the period during which the myocardium contracts and blood is ejected from the ventricle, and diastole that is, instead, the period when the myocardium is relaxing [6]. At rest diastole takes about two thirds of the entire cardiac period. The most important role in the cardyac cicle is played by the left ventricle, because the right side of the hearth tends to follow the patterns estabilished by the left side.

There are four phases of the ventricular activity that can be defined by the state of the inlet and outlet valves (see [6]); we will focus in the phase useful for this work: the aortic valve opens when the pressure in left ventricle overcomes the pressure in the aorta, starting the *ventricular ejection* phase of the cardiac cycle. At this point the vessels begin to expand because of the blood ejected from the hearth and then the aortic pressure begins to rise. However as long as the myocardium is contracting quickly enouhg, the ΔP (pressure difference) between the left ventricle and aorta remains negative and for this reason the blood's flow into the aorta keep accelerating. After a short time the rate of contraction of the ventricle becomes less than the flow rate of blood in the aorta and at that point the pressure difference between left ventriculus and aorta becomes about zero and that moment coincide with the moment of maximum flow rate into the aorta. See Figure 1.2 in which it can appreciate that the duration of this phase is about $0.25s$.

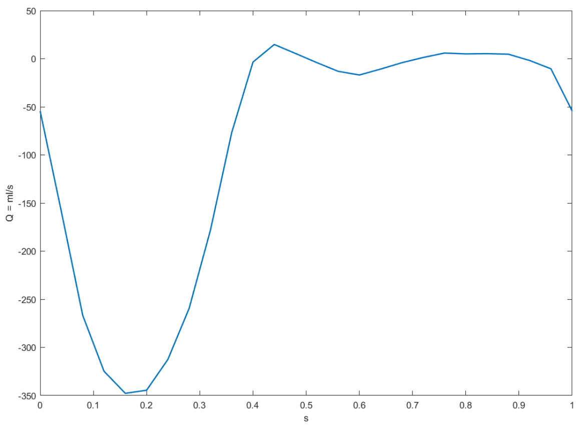

Figure 1.1: Blood flows vs time during a single cardiac cycle

Note, in the Figure 1.1, that the flow is negative because by convention the circulatory system is measured in the direction of mean blood flow; moreover from the 1.1 the reader can appreciate the peak flow that manifests itself bewteen about $0.1s$ and $0.2s$ and so it confirms that the duration of the ventricular ejection amounts to proximately 0.25 as said before.

Note that when we will introduce VAD and we will analyze the problem of the sick patient the device will no longer provide a real cardiac cycle with systole and diastole, in fact the pump will inject the blood into the aorta with a constant flow rate, which will be one of the study parameters of this work.

1.2 State of the art on VAD technology

Ventricular assist devices (VAD) have been developed to assist the heart issues firstly as a step towards transplantation, but more recently as a step towards recovery. A generic VAD is a mechanical pump, also called *artificial heart*, which replaces the function of the left ventricle (most of the time - in this case it is called LVAD), of the right ventricle (RVAD), or both (BIVAD), to increase the amount of blood in the circulation. The device is implanted at the tip of the heart, while the control unit and the battery of the device are located outside the body [50]. The use of LVADs has been associated with an increased risk of thrombus formation in the aortic region because of the formation of stagnation points and recirculation zones; indeed, while first generation devices provided pulsatile flows, current LVADs produce continuous flow (cf-LVADs). This constant flow to the aortic root may lead to decreased excursion or even complete closure of the aortic valve (AV), particularly at high pump speeds. The resultant stasis in the aortic root forms a nidus for clot formation. Aortic root thrombosis has been recognized as a major complication of cf-LVAD therapy which frequently necessitates device exchange in eligible patients to restore forward flow and prevent embolic stroke [42, 43, 44, 35]. A small incision in the abdomen allows the passage of the connection cable. The device aspirates oxygen-rich blood from the left ventricle to push it into the aorta through an artificial vessel (called *graft*)[34]. Once the blood has reached the aorta, it is able to flow to the rest of the body. The use of a VAD is usually considered in case of very advanced heart failure to accompany the patient in the best possible conditions towards heart transplantation: this kind of intervention is, in fact, called *bridge to transplant*. [45]

Thanks to increasingly advanced technology capable of producing smaller and smaller devices, today VAD are also used as permanent therapy, the so-called *destination therapy* [46,47], a possibility for subjects who cannot be transplanted for clinical reasons.

The modern VAD technology provides devices with actively pump blood from the ventricle to the aorta, these devices can be considered turbine pumps that mimic the fucntioning of the LV; the turbine pumps are the most recent development [48].

For the objectives of this work, we will only analyze LVADs.

A LVAD device includes:

- a pump inserted and connected to the left ventricle;
- an external control unit, consisting of a small computer that monitors the pump;
- an operating cable, which connects the pump to the control unit.
- power supplies that operate the pump and the control unit.

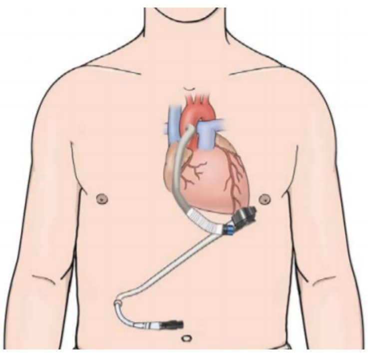

Figure 1.2: Example of positioning the VAD

As we can see from Figure 1.2 the LVAD uses a rotary blood pump to generate flow and assist the left ventricle. It is a centrifugally-configured device so that the paths of the entering and exiting flow stream are perpendicular to the pump axis.

Chapter 2

Mathematical model

In this chapter, we introduce the analytical model apt to describe the behavior of an incompressible viscous Newtonian fluid, i.e. Navier-Stokes equations. We will expose and analyze the main hypotheses concerning the mathematical model and we will give more specific descriptions about the fluid dynamic characteristics of the fluid under consideration in this work, the blood. Once the hypotheses are defined, we will show the equations on which our analytical model is based and the changes applied in relation to the assumptions made, finally we will analyze the boundary conditions of the model.

2.1 Hypothesis on the Mathematical Model

The properties of the fluid must be clarified in relation to the interaction with the surroinding domain; in this case the blood can change, even considerably, its fluid dynamic behaviour depending on the blood vessel in which it flows [6].

Blood contains living cells and plasma, plasma takes up about 55% of the blood volume, while the remaining volume is made up of cells, about 97 % of this remaining volume is made up of erythrocytes (red blood cells) [6].

Red blood cells are the most numerous and therefore they are the ones that mainly discriminate the mechanical and therefore fluid dynamic behaviors of the blood: blood is a *shear-thinning* fluid (see [7]), a fluid the more it shakes the more it fluidifies.

A *shear-thinning* fluid is a fluid whose *viscosity* decreases as the *rate of deformation* increases, and this effect is more pronounced in the gradually smaller blood vessels, because in them the red blood cells are placed and move in the central part of the vessel, while the plasma is positioned externally staying in contact with the vessel wall, clearly this layer of plasma eases the movement of red blood cells, causing a decrease in viscosity (see [8]).

Let us assume some simplifying hypotheses of the mathematical model:

- we will consider blood as a *Newtonian Fluid* (see Section **2.2**), so in the model we will neglect the *shear thinning* effects; this hypothesis is justified by the fact that in the larger blood vessels (and in our case we will work with the Aorta which is the largest artery in the human body) the contribution of non-Newtonian blood behavior can be neglected [6], in addition, in general, non-Newtonian blood behaviors can be neglected when one is interested in the medium flow and not in the deeper details of the flow itself;

- we will neglect the so-called *fluid-structure interaction* effects; this too is not a seemingly realistic hypothesis, since the human cardiovascular system should not be considered as a system of pipes in which blood flows. In fact blood vessels deform according to contingent needs, so there is a *fluid-structure interaction* in the flow of blood through the blood vessels (see [9]), however it can be shown that in the type of simulations we will do in this work, the effects of *fluid-structure interaction* can be neglected [6].

- we will consider blood as an incompressible flow

At this point we are ready to preset more deeply the mathematical model adopted for the problem under consideration in this thesis.

2.2 Navier-Stokes equations

The mathematical equations of fluid dynamics are one of the main components of haemodynamics modelling [6]. In this section, we introduce the analytical mathematical model suitable to describe an incompressible viscous Newtonian fluid: the *Navier-Stokes equations* [8]. As we said before, we consider the blood as a constant density incompressible Newtonian fluid.

In general, in a Newtonian incompressible fluid, the stress tensor (also called Cauchy stress tensor) and the strain rate have a linear dependence, in formulas:

$$\sigma = \sigma(\mathbf{u}, P) = -P\mathbf{I} + 2\mu\mathbf{D}(\mathbf{u}) = -P\mathbf{I} + \mu(\nabla\mathbf{u} + \nabla\mathbf{u}^{\mathbf{T}}), \tag{2.1}$$

where P is the pressure and μ is the *dynamic viscosity* of the fluid. The term $2\mu\mathbf{D}(\mathbf{u})$ is the viscous stress component of the stress tensor. Since we have decided to consider blood as a Newtonian fluid, the viscosity μ is independent of any *kinematic quantitites*, if instead we had also taken into account the non-Newtonian part of the blood we would have had to express the viscosity as a function of the strain rate, namely:

$$\mu = \mu(\mathbf{D}(\mathbf{u})).$$

At this point, in order to obtain the *Navier-Stokes equations*, we use two conservation principles:

- mass conservation;
- momentum conservation.

2.2.1 Mass conservation equation

If ρ is the density of a continuum medium, the equation of mass conservation is:

$$\frac{\partial\rho}{\partial t} + \nabla\cdot(\rho\mathbf{u}) = 0 \quad in \;\; \Omega(t). \tag{2.2}$$

If, as previously mentioned, we assume that blood is an incompressible fluid and therefore with constant density ρ, the equation (2.2) becomes:

$$\nabla\cdot\mathbf{u} = 0 \quad in \;\; \Omega(t), \tag{2.3}$$

so the equation of contintuity (2.2), in the case of incompressible fluid, is reduced to a zero divergence condition of the velocity field $\mathbf{u}$ (see (2.3)).

2.2.2 Momentum conservation equation

At this point we take into consideration the generic principle of momentum conservation for a generic continuous medium (this is a generalization of Newton's second law):

$$\rho\frac{\partial \mathbf{u}}{\partial t} + \rho(\mathbf{u}\cdot\nabla)\mathbf{u} - \nabla\cdot\sigma = \rho\mathbf{f} \quad in \quad \Omega(t) \quad t>0. \tag{2.4}$$

The (2.4) equation can also be expressed in the so-called conservation form:

$$\frac{\partial(\rho\mathbf{u})}{\partial t} + \nabla\cdot(\rho\mathbf{u}\otimes\mathbf{u} - \sigma) = \rho\mathbf{f} \quad in \quad \Omega(t) \quad t>0. \tag{2.5}$$

To get to the Navier-Stokes equations we must first replace the tensor σ to the equation (2.4) (or to the (2.5)), so substituting the (2.1) in the (2.5), remembering that ρ is a constant, we obtain:

$$\rho\frac{\partial \mathbf{u}}{\partial t} + \nabla\cdot(\rho\mathbf{u}\otimes\mathbf{u}) + \nabla P - 2\nabla\cdot(\mu\mathbf{D}(\mathbf{u})) = \rho\mathbf{f}. \tag{2.6}$$

By taking advantage of the fact that ρ is constant we can divide the equation (2.6) by ρ, by introducing a new type of viscosity: $\nu = \frac{\mu}{\rho}$, called *kinematic viscosity*, a scaled pressure $P = \frac{P}{\rho}$, we obtain:

$$\frac{\partial \mathbf{u}}{\partial t} + \nabla\cdot(\mathbf{u}\otimes\mathbf{u}) + \nabla P - \nabla\cdot[\nu(\nabla\mathbf{u} + \nabla\mathbf{u}^{\mathbf{T}})] = \mathbf{f}. \tag{2.7}$$

At this point we have all the elements to be able to express Navier-Stokes equations, in the case of incompressible Newtonian fluid:

$$\begin{cases} \dfrac{\partial \mathbf{u}}{\partial t} + \nabla\cdot(\mathbf{u}\otimes\mathbf{u}) + \nabla P - \nabla\cdot[\nu(\nabla\mathbf{u} + \nabla\mathbf{u}^{\mathbf{T}})] = \mathbf{f}, \\ \nabla\cdot\mathbf{u} = 0. \end{cases} \tag{2.8}$$

As previously described, the first equation is a manipulation of the momentum balance equation and is essentially a reformulation of Newton's 2nd law of dynamics, in which the addends represent: $\dfrac{\partial u}{\partial t}$ is the Eulerian acceleration of the fluid, the term $\nabla\cdot(\mathbf{u}\otimes\mathbf{u})$ models the convection part, the term ∇P is the pressure gradient and finally $\nabla\cdot[\nu(\nabla\mathbf{u} + \nabla\mathbf{u}^{\mathbf{T}})]$ models the diffusion part. The second equation, instead, as explained above, is the mass balance equation (also called continuity equation) for an incompressible fluid.

Physycal quantities of interest

For the sake of convenience, we also define the viscous stress tensor τ as follows:

$$\tau(\mathbf{u}) = \mu(\nabla\mathbf{u} + \nabla\mathbf{u}^T). \tag{2.9}$$

In order to investigate the blood flow patterns, we introduce the Wall Shear Stress (WSS) defined in the following way:

$$WSS = \tau_\omega \cdot \mathbf{n}, \tag{2.10}$$

where $\mathbf{n}$ is the unit normal vector. When the flow is pulsatile, it is useful to make reference to the Time Averaged WSS (TAWSS),

$$TAWSS = \frac{1}{T}\int_0^T WSS dt. \tag{2.11}$$

Finally, in order to characterize the flow regime under consideration, we define the Reynolds number as:

$$Re = \frac{UL}{\nu}, \tag{2.12}$$

where ν is the *kinematic* viscosity previously defined, and U and L are characteristic macroscopic velocity and length, respectively.

2.3 Boundary conditions

Boundary conditions are essential in order to obtain correct cardiovascular simulation results. It is crucial that boundary conditions capture as much as possible the physiology of vascular networks outside of the 3D domain of the model.

Regardless of the complexity of the domain in a vascular model, boundaries can be classified into three macro-categories:

- an inflow boundary, which includes all the faces of the bounary in which we will prescribe a flow wave profile obtained through clinical measurement by medicals [22];
- vessel wall boundary that represents the interface between the fluid domain and the vessel wall. From a physical point of view, this boundary is flanked by a layer of endothelial cells, and the treatment of this layer of cells could be, in general, complex; the most of blood flow simulations, including that considered in this discussion, have traditionally used a rigid wall assumption, in which a zero velocity condition is applied on these surfaces, the so-called *no slip condition* [22];
- an outflow boundary: on this boundary, we will typically prescribe a pressure value that is uniform over the face (spatially costant).

For a generic cardiovascular flow could be considered several options for boundary condition assignment [3], in this work we will consider an inlet boundary in which we will prescribe a precise speed profile (so we will set a Dirichlet condition for speed), we will consider the vessel wall boundary as a rigid wall and then we will impose the *no slip condition* for the speed, while for all the other boundaries (which we will list later) we will impose the so-called *aortic outflow boundary condition*, i.e. we will make an analogy to electrical circuits in which pressure drop is modeled with resistors and vessel distensibility is modeled with capacitors, this electrical analogy is usually called Windkessel RCR boundary conditions (see [10]).

2.3.1 Windkessel RCR boundary conditions

A Windkessel model is composed by three elements: a proximal resistance that modeling the viscous resistance of the arterial vasculature just downstream of the model, a capacitor which models the vessel compliance of all the downstream vasculature, and the distal resistance which models the resistance of the other capillaries and venous circulation. The goal of this parameters-setting is to obtain pressure results that match as much as possible with the patient-specific physiologic conditions, clearly if the patient-specific data are available it is easier set these parameters, otherwise it is sometimes necessary to search for values obtained in the literature. A procedure for obtaining these parameters can be the following:

- calculate the total resistance for the system, this can be done by dividing the patient's average pressure P by the patient's cardiac output Q, in formulas:
$$R_{tot} = \frac{P_{mean}}{Q};$$

- at this point we split the resistance value; as we can see from the figure 2.1, R_p models the proximal resistance while R_d (distale resistance) models the resistance of capillaries and veins; the figure 2.1 also shows that the resistance R_d is more distant from the outflow than the resistance R_p. A good rule of thumb for dividing R_{tot} is the ratio $\frac{R_d}{R_p} \sim 10$. This is due to the fact that most vascular resistance is packed into the downstream vasculature [22], where the small capillaries are. In the case in which there are multiple outlet faces of the domain, such as the case under consideration in this work, we can split the resistances following the rules of a parallel electric circuit (we will analyze more deeply this concept in the next subsection); we will assume that outlets with larger cross sectional area will have less resistance than the smaller outlets, in formulas:
$$R_i = \frac{\sum_j A_j}{A_i} R_{tot},$$
where $\sum_j A_j$ is the sum of the areas of the boundaries that we are taking into account to compute the resistance;

- capacitors model vessel compliance, i.e. the ability for blood vessels to expand and contract in response to blood flow. Determining a value for this parameter is often very complicated, in fact we often take refuge in values obtained in the literature, a very interesting study may be an inference analysis on this parameter. Also in the case in which there are multiple outlet, we can split the capacities similarly to the case of resistences (we will analyze this concept more deeply in the next section), with the difference that in parallel circuits the multiplication coefficient is inverse, that is $\frac{A_i}{\sum_j A_j}$.

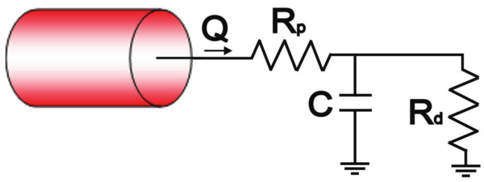

Figure 2.1: RCR Windkessel model

Experimental measurements obtained by the *RHC* and *ECHO* tests are reported in Tables 2.1 and 2.2 for pre-surgery and post-surgery configuration respectively. They are used in order to enforce realistic boundary conditions. For clinical reasons, four different tests are available for the post-surgery configurations whilst only one for the pre-surgery configuration. Note that *RCH* and *ECHO* tests provided measurements related to the polmonary circulation as well. However, these data are not reported because they do not affect the model used in this work, that deals with the systemic compartment only. In Table 2.3 we report the values of boundaries cross-sectional areas.

In the pre-surgery configuration, a realistic flow rate Q waveform was enforced on the ascending aorta section (Figure 1.1). The amplitude of the flow waveform has been set according to the average flow over the cardiac cycle, CO,

$$CO = \frac{1}{T}\int_0^T Qdt, \tag{2.13}$$

measured by the RHC test. The value of the cardiac period, T, is obtained as:

$$T = \frac{SV}{CO}, \tag{2.14}$$

where SV is the stroke volume measured by the ECHO test.

On the other hand, in the post-surgery configuration, the LVAD flow rate, PF, has been used as inlet boundary condition applied to the outflow cannula section. Note that the aortic valve is closed during all the cardiac cycle, i.e. the cardiac flow rate is supplied by the LVAD device only and the ascending aorta section is treated as a wall. In Figure 2.2, the pressure head (ΔP) - volume flow rate (PF) curves for the Heartmate 3^{TM} Left Ventricular Assist System [50] at several pump speed values ω are shown. The basic pump dynamics can, in line of principle, be described in the following way [51]:

$$\Delta P = K_A\omega^2 + K_B\omega \cdot PF + K_C PF^2, \tag{2.15}$$

where K_A, K_B, and K_C are constants which depend on pump design. After some numerical experiments, we found that te coefficients given in Table 2.4 provide an acceptable fit as showed in Figure 2.2. Based on the analytical fitting 11, we can compute the values of ΔP for the all the tests under consideration (see Table 2.5).

PAS [mmHg]	PAD [mmHg]	PAM [mmHg]	CO [l/min]	SV [ml]
108	66	78	5.63	55

Table 2.1: Pre surgery configuration: experimental data obtained by the *RHC* and *ECHO* tests. PAS: systolic arterial pressure, PAD: diastolic arterial pressure, PAM: average arterial pressure, CO: average cardiac flow rate, SV: stroke volume.

	PF [l/min]	ω [rpm]	PAM [mmHg]
Test 1	4.1	5400	78
Test 2	4.2	5600	90
Test 3	4.5	6000	100
Test 4	5	5600	83

Table 2.2: Post-surgery configuration: experimental data obtained by the *RHC* and *ECHO* tests. PF = LVAD flow rate, ω = pump speed, PAM = average arterial pressure.

	A $[cm^2]$
Outflow cannula	1.3
Ascending Aorta	6.42
Right subclavian artery	0.156
Right common carotid artery	0.246
Left common carotid artery	0.168
Left subclavian artery	0.446
Descending aorta	3.68

Table 2.3: Values of boundaries cross-sectional areas.

K_A [mmHg/rpm^2]	K_B [mmHg$\cdot$ l/min/rpm]	K_C [mmHg$\cdot$ l^2/rpm^2]
3.45e-6	-5.9e-5	-1.45

Table 2.4: Parameter settings for the pump dynamics (equation (2.15)).

	ΔP [mmHg]
Test 1	75
Test 2	81.3
Test 3	93.3
Test 4	70.4

Table 2.5: ΔP values based on equation (2.15) for all the tests under consideration.

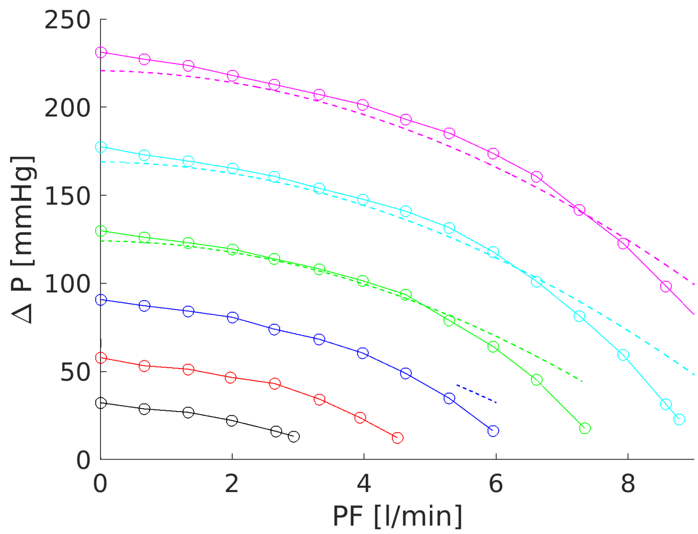

Figure 2.2: Pressure head (ΔP) - volume flow rate (PF) curves (continuous line with circles) and analytical fitting (dashed line) based on equation (2.15) for Heartmate $3^T M$ [50] pump at several pump speed values: ω 3000 rpm (black), ω 4000 rpm (red), ω 5000 rpm (blue), ω 6000 rpm (green), ω 7000 rpm (cyan), ω 8000 rpm (magenta).

Outflow boundary conditions were applied at each outlet of the model, right subclavian artery, right common carotid artery, left common carotid artery, left subclavian artery and descending aorta, by using a three-element Windkessel RCR model [52]. The Windkessel model consists of a proximal resistance $R_{p,k}$, a compliance C_k, and a distal resistance $R_{d,k}$, for each outlet

k (Figure 2.3). The downstream pressure, p_k, is expressed through the following DAE system:

$$\begin{cases} C_k \dfrac{dp_{p,k}}{dt} + \dfrac{p_{p,k} - p_{d,k}}{R_{d,k}} = Q_k, \\ p_k - p_{p,k} = R_{p,k} Q_k, \end{cases} \tag{2.16}$$

where Q_k is the flow rate, and $p_{p,k}$ and $p_{d,k}$ are the proximal and the distal pressure, respectively. The total resistance, $R_k = R_{p,k} + R_{d,k}$, was evaluated according to the rules for a parallel circuit (as mentioned in the previous section):

$$R_k = RVS \frac{\sum_k A_k}{A_k}, \tag{2.17}$$

where A_k is the cross-sectional area and RVS is the systemic vascular resistance estimated as follows:

$$RSV = \begin{cases} \dfrac{PAM}{CO}, & \text{in the pre-surgery case} \\ \\ \dfrac{PAM}{PF}, & \text{in the post-surgety case} \end{cases} \tag{2.18}$$

where PAM is the average arterial pressure measured by the RHC test (see Tables 2.1 and 2.2). For each outlet k, we assumed [53]:

$$\frac{R_{p,k}}{R_k} = 0.056. \tag{2.19}$$

On the other hand, the aortic compliance, C, can be estimated as follows [54]:

$$C = \frac{PAS - PAD}{SV}, \tag{2.20}$$

where PAS and PAD are the systolic and the diastolic pressure measured by the RHC test in the pre-surgery configuration, respectively (see Table 2.1). It should be noted that such value is also used in the post-surgery configuration. Finally, the compliance C_k related to the outlet k was evaluated according to the rules for a parallel circuit (as mentioned in the previous section):

$$C_k = C \frac{A_k}{\sum_k A_k}. \tag{2.21}$$

Table 2.6 shows the values of T, RVS and C computed by using equations: (2.14), (2.18), and (2.20), respectively, for the pre-surgery configuration. Table 2.7 shows the values of RVS computed by using equation (2.18) for the post-surgery configuration. Finally, tables 2.8 and 2.9 report the values of Windkessel parameters for the pre-surgery and post-surgery configurations, respectively.

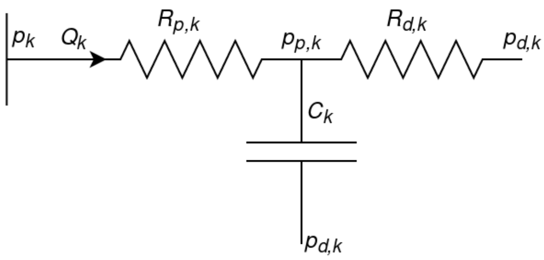

Figure 2.3: Three-element Windkessel model for the generic outlet k.

T [s]	RVS [dyne · s/cm^5]	C [cm^5/dyne]
0.586	1105	9.85e-4

Table 2.6: Pre-surgery configuration: quantities computed by the experimental data reported in Table 2.1. T = cardiac cycle (equation (2.14)), RVS = system vascular resistance (equation (2.18)), C = aortic compliance (equation (2.20)).

	RSV [dyne · s/cm^5]
Test 1	1522
Test 2	1714
Test 3	1778
Test 4	1328

Table 2.7: Post-surgery configuration: system vascular resistance (equation (2.18)) computed by the experimental data reported in Table 2.2 .

k	$R_{p,k}$ [dyne · s/cm^5]	$R_{d,k}$ [dyne · s/cm^5]	C_k [cm^5/dyne]
Right sublcavian artery	1.84e3	3.11e4	3.26e-5
Right common carotid artery	1.23e3	2.07e4	5.16e-5
Left common carotid artery	1.78e3	3.01e4	3.52e-5
Left sublcavian artery	7.09e2	1.19e4	9.35e-5
Descending aorta	7.8e1	1.31e3	7.72e-4

Table 2.8: Pre-surgery configuration Windkessel parameters: proximal resistance $R_{p,k}$, distal resistance $R_{d,k}$ and compliance C_k, for each outlet k.

	k	$R_{p,k}$ [dyne · s/cm^5]	$R_{d,k}$ [dyne · s/cm^5]
Test 1	Right sublcavian artery	2.56e3	4.32e4
	Right common carotid artery	1.63e3	2.74e4
	Left common carotid artery	2.38e3	4e4
	Left sublcavian artery	8.96e2	1.51e4
	Descending aorta	1.08e2	1.83e3
Test 2	Right sublcavian artery	2.88e3	4.86e4
	Right common carotid artery	1.83e3	3.08e4
	Left common carotid artery	2.68e3	4.51e4
	Left sublcavian artery	1.01e3	1.7e4
	Descending aorta	1.22e2	2.06e3
Test 3	Right sublcavian artery	2.99e3	5.05e4
	Right common carotid artery	1.9e3	3.2e4
	Left common carotid artery	2.78e3	4.68e4
	Left sublcavian artery	1.04e3	1.76e4
	Descending aorta	1.27e2	2.14e3
Test 4	Right sublcavian artery	2.19e3	3.68e4
	Right common carotid artery	1.39e3	2.33e4
	Left common carotid artery	2.03e3	3.42e4
	Left sublcavian artery	7.64e2	1.29e4
	Descending aorta	9.25e1	1.56e3

Table 2.9: Post-surgery configuration Windkessel parameters: proximal resistance $R_{p,k}$ and distal resistance $R_{d,k}$, for each outlet k.

Chapter 3

Full Order Model Formulations

We now discuss the Full Order Model (FOM), which generates what we call the high fidelity solution. Navier-Stokes equations are the most precise continuous model to describe the motion of a fluid but, due to their complexity, it is very difficult, and in most cases impossible, to solve them analytically except in few very simplified cases. For this reason, usually, the only way to solve fluid dynamic problems governed by this set of equations is to discretize them by means of a suitable discretization method, in this work, in particular, we will present the *Finite Element Method* (FEM) with SUPG-stabilization ([49]) and the *Finite Volume Method* (FV) ([55]).

Let us consider a generic domain $\Omega \subseteq R^d$, limited, connected with boundary *sufficiently* regular so that the Gauss divergence theorem can be applied; suppose that this domain Ω is the observation region of the fluid (in our case the blood); as we have already said, the fluid is described by a vector field $\mathbf{u}$ (velocity) and by a scalar field p (kinematic pressure). Considering the system of equations (2.8), in our problem under consideration we will assume that the viscosity ν is constant, so the momentum balance equation changes in its diffusive term $\nabla\cdot[\nu(\nabla\mathbf{u} + \nabla\mathbf{u}^{\mathbf{T}})]$ since, considering ν constant, it can be taken out of the sign of divergence, and therefore we obtain that $\nabla \cdot (\nabla\mathbf{u}) = \Delta\mathbf{u}$ and $\nabla \cdot (\nabla\mathbf{u}^{\mathbf{T}}) = \nabla(\nabla \cdot \mathbf{u}) = \mathbf{0}$, whereby the new set of equations: incompressible Navier-Stokes with boundary conditions and initial condition, become:

$$
\begin{cases}
\dfrac{\partial \mathbf{u}}{\partial t} + (\mathbf{u}\cdot\nabla)\mathbf{u} + \nabla P - \Delta\mathbf{u} = \mathbf{f}, \quad in\ \Omega \times (0,T]\ \ T > 0, \\
\nabla \cdot \mathbf{u} = 0, \quad in\ \Omega \times (0,T]\ \ T > 0, \\
\mathbf{u} = \mathbf{g}, \quad in\ \partial\Omega \times (0,T]\ \ T > 0, \\
\mathbf{u}(\mathbf{0}) = \mathbf{u_0}, \quad in\ \Omega.
\end{cases}
\tag{3.1}
$$

If one only looked at the part of the equation $\dfrac{\partial \mathbf{u}}{\partial t}$ -$\boldsymbol{\Delta}\mathbf{u} = \mathbf{f}$ we would have a parabolic equation (like heat equation) vectorial, however there is the term $(\mathbf{u}\cdot\nabla)\mathbf{u}$, which is the convection term that provides the nonlinearity of the equation and then there is the term $\nabla\mathbf{P}$ which is a term linked to the constraint of incompressibility $\nabla \cdot \mathbf{u} = 0$.

The mathemathical steps that lead the convective term to the form in (3.1) are presented below:

$$
\nabla \cdot (\mathbf{u}\mathbf{u}^{\mathbf{T}}) = (\mathbf{u}\cdot\nabla)\mathbf{u} + \mathbf{u}(\nabla\cdot\mathbf{u}) = (\mathbf{u}\cdot\nabla)\mathbf{u}, \tag{3.2}
$$

in the last equality we have exploited the solenoidity constraint of the velocity field $\mathbf{u}$.

3.1 Finite Element Method

The finite element method (FEM) is a numerical technique for solving problems described by partial differential equations. The goal of this method is to determine approximating functions that are determined in terms of nodal values of the physical field of interest. A continuous mathematical problem is transformed into a discretized finite element problem with unknown nodal values.

3.1.1 Weak formulation of Navier-Stokes Equations

A preparatory passage for finite element discretization of the system of equations presented in (3.1) is to obtain the weak formulation of the system, before proceeding we recall some concepts of functional analysis that will be useful in the following:

Definition 1. *We define the following function spaces:*

$$L^2(\Omega) = \{v : \Omega \to C \ : \ ||v||_{L^2(\Omega)} = \left(\int_\Omega |v|^2 dx\right)^{\frac{1}{2}} < \infty\},$$

$$H^1(\Omega) = \{v : \Omega \to C \ : v \in L^2(\Omega) \ , \ \nabla v \in (L^2(\Omega))^d\},$$

$$H_0^1(\Omega) = \{v : \Omega \to C \ : v \in H^1(\Omega) \ : \ v = 0 \in \ \partial\Omega\},$$

$$H^{\frac{1}{2}}(\partial\Omega) = \{g : \partial\Omega \to C \ : g = v_{|\{\partial\Omega} : v \in H^1(\Omega)\}.$$

Taking advantage of Poincarè inequality ([11]) applied to the domain Ω, we can consider the following equality between norms that could be useful to us in the following:

$$||v||_{H_0^1(\Omega)} = ||\nabla v||_{L^2(\Omega)^d}.$$

Another definition that will be very useful to us is the one of *dual space*:

Definition 2. *Let V be a Banach space ([12]), we define dual space V', the set of all linear and continuos functionals $F : V \to C$.*

In particular for our work, we will need the dual space $(H_0^1(\Omega))' := H^{-1}(\Omega)$.

3.1.2 Functional framework

At this point we have all the elements to be able to characterize the functional treatment of each of the terms of the Navier-Stokes equations:

- suppose that the vector field $\mathbf{u}(x, t)$ consists of a series of functions all defined in the domain Ω, which vary with the variation of time t, for which we rewrite $(\mathbf{u}(t))(\mathbf{x})$ and assume that:

$$\mathbf{u} \in L^2(0, T; (H^1(\Omega))^d);$$

- we consider Laplacian as a continuous operator:

$$\Delta : H^1(\Omega) \to H^{-1}(\Omega),$$

which acts as follows, let $v \in H^1(\Omega)$ and let $\phi \in H_0^1(\Omega)$, then:

$$\Delta v(\phi) = -\int_\Omega \nabla v \cdot \nabla \phi,$$

so we can assume that:

$$\nabla \mathbf{u} \in L^2(0,T;(H^{-1}(\Omega))^d),$$

- as regards the convective term, with the previous hypotheses, it can be demonstrated that we obtain:

$$(\mathbf{u} \cdot \nabla)\mathbf{u} \in L^2(0,T;(H^{-1}(\Omega))^d),$$

- as for the pressure p, we suppose that:

$$p \in L^2(0,T;L^2(\Omega)),$$

which implies:

$$\nabla \mathbf{p} \in L^2(0,T;(H^{-1}(\Omega))^d),$$

- finally for right-hand-side term $\mathbf{f}$ we suppose that:

$$\mathbf{f} \in L^2(0,T;(H^{-1}(\Omega))^d.$$

In light of the hypotheses presented above, we can rewrite the system equation (3.1):

$$\frac{\partial \mathbf{u}}{\partial t} = \underbrace{-(\mathbf{u} \cdot \nabla)\mathbf{u} - \nabla \mathbf{P} + \nu \boldsymbol{\Delta} \mathbf{u} + \mathbf{f}}_{\in L^2(0;T;(H^1(\Omega))^d)}, \tag{3.3}$$

- from the equation (3.3) it emerges that the time derivative term of the velocity field $\mathbf{u}$ belongs to the same space to which all the right-hand-side of the (3.3), in formulas:

$$\frac{\partial \mathbf{u}}{\partial t} \in L^2(0,T;(H^{-1}(\Omega))^d).$$

In light of the hypotheses made on $\mathbf{u}$ and $\dfrac{\partial \mathbf{u}}{\partial t}$, using the Lions' Theorem (see [11]) we obtain that:

$$\mathbf{u} \ \in C^0([0,T];(L^2(\Omega))^d). \tag{3.4}$$

Thanks to the result obtained in the equation (3.4), considering that the function $\mathbf{u}$ is continuous with respect to the variable time, we can make sense of the evaluation of the function $\mathbf{u}$ in a precise instant of time, thus being able to affirm, regarding the initial condition in the system (3.1), that:

$$\mathbf{u_0} \in (L^2(\Omega))^d,$$

- as regards the boundary conditions (which as can be seen from the system of equations (3.1), we have assumed to be Dirichlet boundary conditions along the whole boundary), we have to analyze the data at the boundary $\mathbf{g}$, for compliance with the previous cases, we assume that:

$$\mathbf{g} \in L^2(0,T;(H^{\frac{1}{2}}(\partial\Omega))^d), \tag{3.5}$$

however, the condition expressed by (3.5) is not enough because if we consider the Gauss divergence theorem we obtain that:

$$\int_\Omega \nabla \cdot \mathbf{u} = \int_{\partial\Omega} \mathbf{u} \cdot \mathbf{n}, \tag{3.6}$$

however for the solenoidal condition that we impose on the velocity field $\mathbf{u}$ due to the hypothesis of incompressible fluid, the first integral of (3.6) is zero, and the second integral is instead calculated along $\partial\Omega$, where $\mathbf{u} = \mathbf{g}$, so from the (3.6) we get an additional constraint for the boundary data $\mathbf{g}$:

$$\int_{\partial\Omega} \mathbf{g} \cdot \mathbf{n} = 0, \tag{3.7}$$

so this condition of compatibility of the data $\mathbf{g}$ with the solenoidal constraint of the velocity field $\mathbf{u}$, translates into requiring that the normal component of the data $\mathbf{g}$ must have zero average on the boundary.

At this point, taking into account (3.5) and the condition (3.7), we can make a dependent variable change for the (3.1) system, introducing a function $\mathbf{u_g} \in (H^1(\Omega))^d$ such that $\mathbf{g} = \mathbf{u_g}$, $\nabla \cdot \mathbf{u_g} = \mathbf{0}$. At this point it is possible to change variables, taking advantage of the $\mathbf{u_g}$ just defined, which is called *edge data detection*; we rewrite $\mathbf{u}$ as:

$$\mathbf{u} = \mathbf{u_g} + \mathbf{u^{(0)}},$$

so we built a new velocity field $\mathbf{u^{(0)}(t)} \in H_1^0(\Omega))^d \quad \forall t \in [0,T]$, which becomes the new unknown of the (3.1) system, precisely:

$$\mathbf{u^{(0)}} \in L^2(0,T;(H_0^1(\Omega))^d).$$

At this point, we presented the whole functional framework in order to obtain the weak formulation of the incompressible Navier-Stokes equations.

The usual procedure for obtaining the weak formulation is to multiply the equation ([14]) in question by a generic test function, so multiplying the first equation of the system (3.1) we obtain the following weak formulation:

$$\int_\Omega \left(\frac{\partial \mathbf{u}}{\partial t} + (\mathbf{u} \cdot \nabla)\mathbf{u} + \nabla p - \Delta \mathbf{u} = \mathbf{f} \right) \cdot \mathbf{v} = 0 \quad \forall \quad \mathbf{v} \in (H_0^1(\Omega))^d, \tag{3.8}$$

where $(H_0^1(\Omega))^d$ represents the space of the test functions.

At this point we analyze again the weak formulation of the Navier-Stokes equations:

- $\displaystyle\int_\Omega \frac{\partial \mathbf{u}}{\partial t} \cdot \mathbf{v} = \frac{d}{dt} \int_\Omega \mathbf{u} \cdot \mathbf{v};$
- the integral $\displaystyle\int_\Omega (\mathbf{u} \cdot \nabla)\mathbf{u} \cdot \mathbf{v}$ is left in this form;

- $-\int_\Omega \boldsymbol{\Delta}\mathbf{u}\cdot\mathbf{v} = +\int_\Omega \nabla\mathbf{u}\cdot\nabla\mathbf{v}$, in this equality we used the integration by parts formula considering the fact that the function $\mathbf{v}$ is null at the boundary;

- $\int_\Omega \nabla\mathbf{p}\cdot\mathbf{v} = -\int_\Omega p\nabla\mathbf{v} + \int_{\partial\Omega} p\mathbf{v}\cdot\mathbf{n} = -\int_\Omega p\nabla\mathbf{v}$,
the last equality is due to the fact that the function $\mathbf{v}$ is null at the boundary;

- $\int_\Omega \mathbf{f}\cdot\mathbf{v}$, also in this case, assuming $\mathbf{f}\in(L^2(\Omega))^d$, the integral is not further manipulated.

.

By putting all the pieces of this formulation together we obtain that the weak formulation of the Navier-Stokes Equations provides that $\forall t\in(0,T]$ we must obtain $\mathbf{u}\in L^2(0,T;(H_0^1(\Omega))^d)$ and $p\in L^2(0,T;L^2(\Omega))$ such that:

$$\begin{cases} \dfrac{d}{dt}(\mathbf{u},\mathbf{v}) + \Big((\mathbf{u}\cdot\nabla)\mathbf{u}),\mathbf{v}\Big) + \mu(\nabla\mathbf{u},\nabla\mathbf{v}) - (p,\nabla\mathbf{v}) = (\mathbf{f},\mathbf{v}) \quad \forall \quad \mathbf{v}\in(H_0^1(\Omega))^d \\ (\nabla\cdot\mathbf{u},q) \quad \forall q\in L^2(\Omega) \end{cases} . \tag{3.9}$$

In (3.9), the symbol $(\cdot)$ represents the scalar product in $L^2(\Omega)$.

3.1.3 Finite Element discretization

For simplicity of notation we will call $V=(H_0^1(\Omega))^d$ e $D=L^2(\Omega)$.

Let us consider a Finite Element partition $\mathcal{T}_h$ of the domain Ω from which we construct finite element spaces $V_h\subset V$ and $D_h\subset D$ ([23]). For the discrete version of equations (3.9) to be well-posed, velocity and pressure spaces V_h and D_h need to obey an inf-sup condition (see [11]):

$$\inf_{q_h\in D_h}\sup_{\mathbf{v_h}\in V_h}\frac{(q_h,\nabla\cdot\mathbf{v_h})}{||\mathbf{v_h}||_V||q_h||_D}\geq\widetilde{\beta}>0, \tag{3.10}$$

at this point, we can present the semi-discrete formulation of the Navier Stokes equation, starting from (3.9) we have that $\forall t\in(0,T]$ we have to obtain $\mathbf{u_h}\in V_h$ e $p_h\in D_h$ such that:

$$\begin{cases} \dfrac{d}{dt}(\mathbf{u_h},\mathbf{v_h}) + \Big((\mathbf{u_h}\cdot\nabla)\mathbf{u_h}),\mathbf{v_h}\Big) + \mu(\nabla\mathbf{u_h},\nabla\mathbf{v_h}) - (p_h,\nabla\mathbf{v_h}) = (\mathbf{f},\mathbf{v_h}) \quad \forall\mathbf{v_h}\in V_h, \\ (\nabla\cdot\mathbf{u_h},q_h) \quad \forall q_h\in D_h. \end{cases} . \tag{3.11}$$

3.1.4 SUPG-stabilization

Since the Galerkin method could lacks stability if convection dominates diffusion, we decided to enrich it by a stabilization, yielding the SUPG (Streamline Upwind Petrov–Galerkin) method. A possible important drawback of many stabilized methods like SUPG is that they contain stabilization parameters for which a general 'optimal' choice could be not known ([22]).

A choice of low-order approximation spaces (such as P1-P1 spaces) seems to represent a very good choice for the apprimation of Navier-Stokes equations, since they apparently decrease the required computational effort([22]); however, they do not satisfy the inf-sup condition (3.10).

As a remedy, one can appeal to suitable pressure stabilizations; however, pressure stabilizations turn out to be inappropriate when dealing with advection dominated flows.

For these reasons, we bring it up the streamline upwind Petrov-Galerkin (SUPG) stabilization – formulated as in the Variational Multiscale framework – which satisfies all the requirements mentioned above.

We introduce the following space:

$$Y_h^r = \{w_h \in C^0(\bar{\Omega}) : w_{h|K} \in P^r \quad \forall K \in \mathcal{T}_h\}.$$

Let us define now: $V_h = V \cap Y_h^r$ e $D_h = D \cap Y_h^r$ and introduce *the residual* respectively of the momentum equation: $\mathbf{r_M}(\mathbf{v_h}, p_h)$ and of the continuity equation: $\mathbf{r_C}(\mathbf{v_h})$ in the following manner:

$$\mathbf{r_M}(\mathbf{v_h}, p_h) = \frac{\partial \mathbf{v_h}}{\partial t} + \mathbf{v_h} \cdot \nabla \mathbf{v_h} + \nabla p - \mu \boldsymbol{\Delta} \mathbf{v_h},$$
$$\mathbf{r_C}(\mathbf{v_h}) = \nabla \cdot \mathbf{v_h}.$$

Putting all the pieces of this formulation back together, the semi-discrete SUPG formulation of the Navier-Stokes equations reads that $\forall t \in (0, T]$ we must obtain $\mathbf{u_h} \in V_h$ e $p_h \in D_h$ such that:

$$\begin{cases} \dfrac{d}{dt}(\mathbf{u_h}, \mathbf{v_h}) + \Big((\mathbf{u_h} \cdot \nabla)\mathbf{u_h}), \mathbf{v_h}\Big) + \mu(\nabla \mathbf{u_h}, \nabla \mathbf{v_h}) - (p_h, \nabla \mathbf{v_h}) + \\ + \sum_{K \in \mathcal{T}} (\tau_M \mathbf{r_M}(\mathbf{v_h}, p_h), \mathbf{v_h} \cdot \nabla \mathbf{w_h} + \nabla q_h)_K + \\ + \sum_{K \in \mathcal{T}} (\tau_C \mathbf{r_C}(\mathbf{v_h}), \nabla \cdot \mathbf{v_h})_K = (\mathbf{f}, \mathbf{v}) \quad \forall \mathbf{v_h} \in V_h \\ (\nabla \cdot \mathbf{u_h}, q_h) \quad \forall q_h \in D_h. \end{cases} \tag{3.12}$$

The stabilization parameter τ_M e τ_C are defined as:

$$\tau_M = \left(\frac{\sigma^2}{(\Delta t)^2} + \mathbf{v_h} \cdot \mathbf{G_k} \mathbf{v_h} + C_I \mu^2 \mathbf{G_K} : \mathbf{G_K} \right)^{-\frac{1}{2}},$$

$$\tau_C = (\tau_M \mathbf{g_K} \cdot \mathbf{g_K})^{-1},$$

where $C_I = 60 \cdot 2^{r-2}$, σ is a constant equal to the order of the time discretization and Δt is the time step that will be chosen for the time discretization. Moreover, $\mathbf{G}_K$ and $\mathbf{g}_K$ are metric tensors of the computational domain [18,19].

3.2 Finite Volume Method

An other possible approach, alternative to the FEM one, to discretize the equations (3.1) is the Finite Volume Method (FVM), for a complete discussion of FVM we refer to texts such as [55] or [56]. Examples of FV application in haemodynamics can be found, e.g., in [85]. FVM approximation is derived directly from the integral form of the governing equations. We have used the finite volume C++ library OpenFOAM® [57]. We partition the computational domain Ω into cells or control volumes Ω_i, with $i = 1, dots, N_c$, where N_c is the total number of cells in the mesh. For simplicity of treatment we rewrite the first equation of the system (3.1) as follows:

$$\rho \frac{\partial \mathbf{u}}{\partial t} + \rho \nabla \cdot (\mathbf{u} \otimes \mathbf{u}) + \nabla p - 2\mu \Delta \mathbf{u} = f \ in \ \Omega \times (t_0, t^*). \tag{3.13}$$

Let $\mathbf{A_j}$ be the surface vector of each face of the control volume.

The integral form of equation (3.13) for each volume Ω_i is given by:

$$\rho \int_{\Omega_i} \frac{\partial \mathbf{u}}{\partial t} d\Omega + \rho \int_{\Omega_i} \nabla \cdot (\mathbf{u} \otimes \mathbf{u}) d\Omega - 2\mu \int_{\Omega_i} \Delta \mathbf{u} d\Omega + \int_{\Omega_i} \nabla p d\Omega = 0. \quad (3.14)$$

By applying the Gauss-divergence theorem, equation (3.14) becomes:

$$\rho \int_{\Omega_i} \frac{\partial \mathbf{u}}{\partial t} d\Omega + \rho \int_{\partial\Omega_i} (\mathbf{u} \otimes \mathbf{u}) \cdot d\mathbf{A} - 2\mu \int_{\partial\Omega_i} \nabla \mathbf{u} \cdot d\mathbf{A} + \int_{\partial\Omega_i} p d\mathbf{A} = 0. \quad (3.15)$$

Each term in equation (3.15) is approximated as follows:

- *Gradient term*:

$$\int_{\partial\Omega_i} p d\mathbf{A} \simeq \sum_j p_j \mathbf{A}_j, \quad (3.16)$$

  where p_j is the value of the pressure relative to centroid of the j^{th} face. The face center pressure values p_j are obtained from the cell center values by means of a linear interpolation scheme.

- *Convective term*:

$$\int_{\partial\Omega_i} (\mathbf{u} \otimes \mathbf{u}) \cdot d\mathbf{A} \simeq \sum_j (\mathbf{u}_j \otimes \mathbf{u}_j) \cdot \mathbf{A}_j = \sum_j \phi_j \mathbf{u}_j, \qquad \phi_j = \mathbf{u}_j \cdot \mathbf{A}_j, \quad (3.17)$$

  where $\mathbf{u}_j$ is the fluid velocity relative to the centroid of each control volume face. In (3.17), ϕ_j is the convective flux associated to $\mathbf{u}$ through face j of the control volume. The convective flux at the cell faces is obtained by a linear interpolation of the values from the adjacent cells. Also $\mathbf{u}$ needs to be approximated at cell face j in order to get the face value $\mathbf{u}_j$. Different interpolation methods can be applied: central, upwind, second order upwind and blended differencing schemes [58]. In this work, we make use of a second order upwind scheme.

- *Diffusion term*:

$$\int_{\partial\Omega_i} \nabla \mathbf{u} \cdot d\mathbf{A} \simeq \sum_j (\nabla \mathbf{u})_j \cdot \mathbf{A}_j, \quad (3.18)$$

  where $(\nabla \mathbf{u})_j$ is the gradient of $\mathbf{u}$ at face j. We are going to briefly explain how $(\nabla \mathbf{u})_j$ is approximated with second order accuracy on structured, orthogonal meshes, that are used in this work. Let P and Q be two neighboring control volumes. The term $(\nabla \mathbf{u})_j$ is evaluated by subtracting the value of velocity at the cell centroid on the P-side of the face, denoted with $\mathbf{u}_P$, from the value of velocity at the centroid on the Q-side, denoted with $\mathbf{u}_Q$, and dividing by the magnitude of the distance vector $\mathbf{d}_j$ connecting the two cell centroids:

$$(\nabla \mathbf{u})_j \cdot \mathbf{A}_j = \frac{\mathbf{u}_Q - \mathbf{u}_P}{|\mathbf{d}_j|} |\mathbf{A}_j|. \quad (3.19)$$

For non-structured, non-orthogonal meshes (see Fig. 5), an explicit non-orthogonal correction has to be added to the orthogonal component in order to preserve second order accuracy. See [58] for details.

A partitioned approach has been used to deal with the pressure-velocity coupling. In particular a Poisson equation for pressure has been used. This is obtained by taking the divergence of the momentum equation (3.13) and exploiting the divergence free constraint $\nabla \cdot \mathbf{u} = 0$:

$$\Delta p = -\nabla(\mathbf{u} \otimes \mathbf{u}). \tag{3.20}$$

The segregated algorithms available in OpenFOAM® are SIMPLE [59] for steady-state problems, and PISO [60] and PIMPLE [61] for transient problems. For this work, we choose the PISO algorithm.

3.3 Time discretization

To discretize in time the equation (3.15), let $\Delta t \in \mathbb{R}$, $t^n = t_0 + n\Delta t$, with $n = 0, \ldots, N_T$ and $t^* = t_0 + N_T\Delta t$. Moreover, we denote by $\mathbf{u}^n$ the approximation of the flow velocity at the time t^n. We adopt Backward Differentiation Formula of order 1 (BDF1), for example see [62]. Given $\mathbf{u}^n$, for $n \geq 0$, we have, respectively,:

$$\frac{\partial \mathbf{u}}{\partial t} \simeq \frac{\mathbf{u}^{n+1} - \mathbf{u}^n}{\Delta t}. \tag{3.21}$$

Finally, a first-order scheme is also used for the discretization of the RCR Windkessel model (2.16):

$$\begin{cases} C_k \dfrac{p_{p,k}^{n+1} - p_{p,k}^n}{\Delta t} + \dfrac{p_{p,k}^{n+1}}{R_{d,k}} = Q_k^n, \\ p_k^{n+1} - p_{p,k}^{n+1} = R_{p,k} Q_k^n, \end{cases} \tag{3.22}$$

where we assumed $p_{d,k} = 0$.

3.3.1 Multi-scale coupling

The coupling process between the three-dimensional flow model and lumped Windkessel model can be summarized as follows:

- At t^n, we know $\mathbf{u}^n$ and thus Q_k^n. Then we calculate p_k^{n+1} by equation (3.22);
- We solve the problem descrived by equations (3.15) to obtain $\mathbf{u}^{n+1}$ and Q_k^{n+1}.

3.4 FEM and FVM comparison: healthy case

After presenting the two discretization techniques in the previous sections: FEM and FVM, in this section we will consider computational simulations obtained with both methods. The domain taken under consideration is an Aorta artery reconstructed from CT images of a healthy patient by using the open source medical image analysis software 3D Slicer ®(**http://www.slicer.org**). We will compare these two methods by confronting the values along the domain of quantities like *time-average pressure*, *wall shear stress*, *magnitude of velocity* and with the help of plots and tables. As we can see from the figure 1.1 an entire cardiac cycle lasts about

1 second; in these simulations we will simulate 10 seconds, so 10 cardiac cycles. For the time discretization we will adopt the discretizazion tecnicque explained in section 3.3.

Clearly the simulations that we are going to compare will be done on the same mesh.

3.4.1 Numerical Results

Mesh

The simulation are computed with a mesh with 600k elements. The mesh is shown in the figure 3.1:

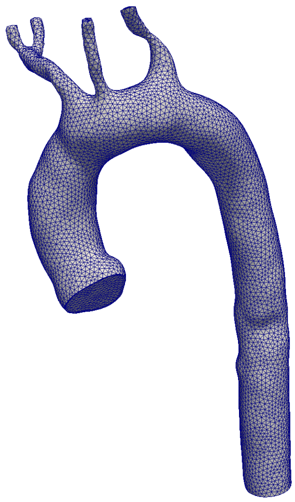

Figure 3.1: View of the mesh 600k.

Boundary conditions

As explained in the previous sections outflow boundary conditions were applied at each outlet of the model, right subclavian artery, right common carotid artery, left common carotid artery, left subclavian artery and descending aorta, by using a three-element Windkessel RCR model. The values are reported in the table 3.1

k	$R_{p,k}$ [dyne $\cdot$ s/cm^5]	$R_{d,k}$ [dyne $\cdot$ s/cm^5]	C_k [cm^5/dyne]
Right sublcavian artery	1.04e3	1.63e4	8.74e-5
Right common carotid artery	1.18e3	1.84e4	7.70e-5
Left common carotid artery	1.18e3	1.84e4	3.52e-5
Left sublcavian artery	9.7e2	1.52e4	9.34e-5
Descending aorta	1.88e2	2.95e3	4.82e-4

Table 3.1: Healthy case configuration, Windkessel parameters: proximal resistance $R_{p,k}$, distal resistance $R_{d,k}$ and compliance C_k, for each outlet k.

The unique inlet of the model is the aortic wall in which we set the aortic inflow waveform described in Figure 1.1.

FEM vs FVM numerical results

In this section we compare the numerical results obtained with the FEM and FVM:

- first of all we compare the plot *pressure* - *time* for both the methods and in the figure 3.2 we can appreciate that the plots are pratically identical:

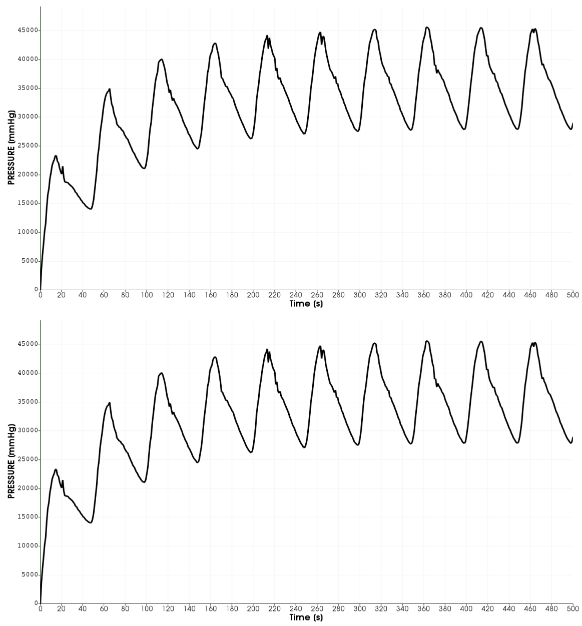

Figure 3.2: Pressure-time plot for the FVM simulation (up figure), and FEM simulation (down figure).

At this point for the following comparation we will compare the time average pressure distribution along the whole surface of our domain. After this we will choice a specific time step of the time discretization at which we will compare the *wall shear stress* distribution along the whole surface of our domain obtained with the two methods. Finally we will choice three slices along the domain in which we will compare the *magnituide of velocity* obtained with the two methods.

- In the figure (3.3) we can appreciate the pratically identical distribution of the *time-average pressure* along the whole domain surface.

Figure 3.3: Time-average pressure distribution for the FVM simulation (left), FEM simulation (right).

In the table 3.2, are reported the numerical values of the *time-average pressure* averaged respect to the whole volume of the domain:

$Volume$ = 139.942 cm^3	Time-averaged pressure [$dyne \cdot cm/s$]
FEM	139779.33
FVM	140540.37
Relative error	0.54%

Table 3.2: Time-averaged pressure, FEM and FVM.

- In the figure (3.4) we can appreciate the pratically indentical distribution of the *wall shear stress* along the whole domain surface:

Figure 3.4: Magnitude velocity distribution for the FVM simulation (left), FEM simulation (right).

- For the comparison with the *magnitude of velocity*, since this quantity is clearly zero along the whole surface, we will choice a slice of the domain in which analyze the comparison between the two methods, the slice (shown in figure 3.5) is taken in the upper part of the descending aorta near the aortic arch.

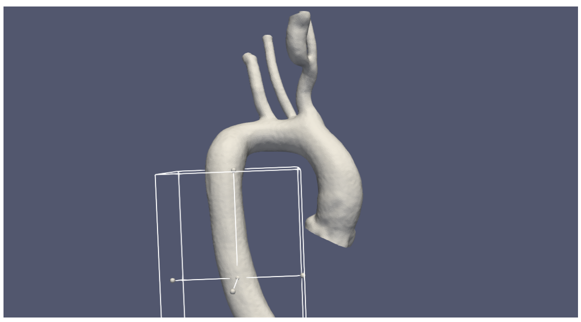

Figure 3.5: Slice of the domain chosen for the magnitude of velocity comparison.

In the figure (3.6) we can appreciate the very similar distribution of the *magnitude of velocity* along the slice shown in 3.5:

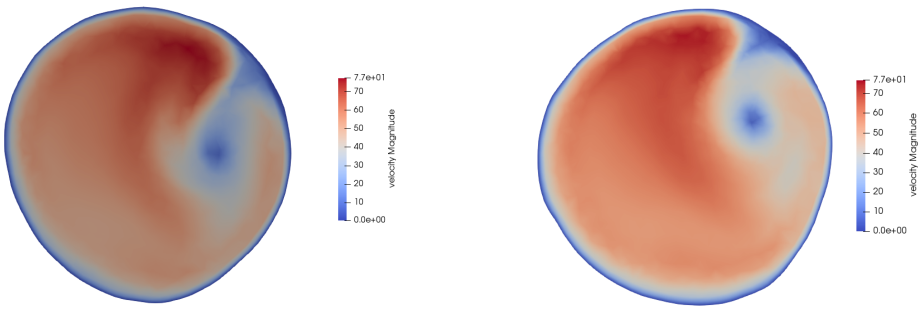

Figure 3.6: Magnitude velocity distribution for the FVM simulation (left), FVM simulation(right).

In the table 3.3, the numerical values of the *magnitude of velocity* averaged respect to the whole area of the slice are reported:

$Area = 4.892\ cm^2$	*Magnitude of velocity* $[1/cm \cdot s]$
FEM	22.3152
FVM	22.1614
Relative error	0.69%

Table 3.3: Magnitude of velocity, FEM vs FVM.

Having ascertained the fact that both methods lead to very similar results, for the continuation of the work we choose to work with the FVM, in that, having to do with flows characterized by relatively high Reynolds numbers, FVM do not lead to stabilization problems unlike FEM.

3.5 Unhealthy patient analysis case

From now on, in this work a patient, a 66 years old man, is considered. CT, RHC and ECHO tests have been carried out both in pre-surgery and post-surgery (i.e., after receiving the LVAD device) configuration. The LVAD implanted is the Heartmate 3^{TM} Left Ventricular Assist System [50].

Real patient-specific aorta models were reconstructed from CT images by using 3D Slicer®. The models include the ascending aorta, brachiocephalic artery, right subclavian artery, right common carotid artery, left common carotid artery, left subclavian artery and descending aorta, and, in the post-surgery configuration, the outflow cannula of the LVAD device as well, as shown in Figure 3.7.

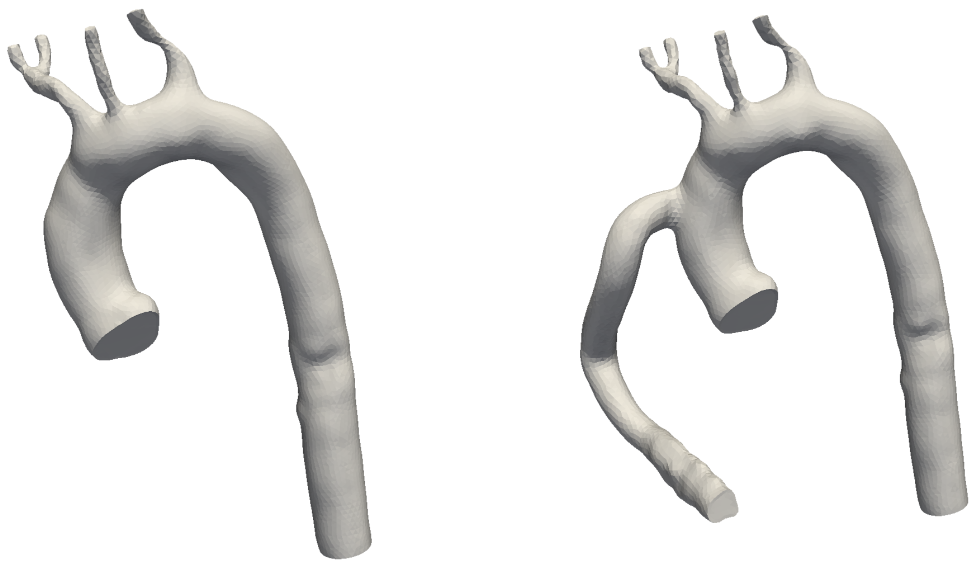

Figure 3.7: Patient specific aorta models obtained from CT images: (left) Pre-surgery configuration, (right) Post-surgery configuration.

3.5.1 Full Order Model validation

The number of PISO loops and non-orthogonal correctors has been fixed to 2 for all the simulations. The following solvers have provided a good compromise between stability, accuracy, and numerical cost. The linear algebraic system associated with equation (3.15) is solved using an iterative solver with symmetric Gauss-Seidel smoother. Moreover, for Poisson problem (3.20), we use Geometric Agglomerated Algebraic Multigrid Solver GAMG with the Gauss-Seidel smoother. The required accuracy is 1e-6 at each time step.

Mesh convergence

In order to obtain grid independent solutions, we consider three meshes with tetrahedral elements. Table 3.4 reports name, minimum and maximum diameter, and number of cells for each mesh. Figure 3.8 shows the mesh 230k. All the meshes under consideration have very low values of average non-orthogonality (around 30 degrees) and skewness (around 1). The estimation of the Reynolds number is based on the diameter computed by considering the inlet areas, i.e. the ascending aorta (ao) section in the pre-surgery configuration and the outflow cannula section (oc) in the post-surgery configuration, as circular areas. We have:

$$Re = \frac{\frac{Q}{A_{ao}}\sqrt{\frac{4A_{ao}}{\pi}}}{\nu} \tag{3.23}$$

$$Re = \frac{\frac{PF}{A_{oc}}\sqrt{\frac{4A_{oc}}{\pi}}}{\nu} \tag{3.24}$$

for the pre-surgery and post-surgery configuration, respectively. We carry out the mesh convergence study for the pre-surgery configuration because it is more critical with respect to the the post-surgery configuration being characterized by a greater Reynolds number Re as showed in Table (3.5). Moreover, note that in the pre-surgery configuration the Reynolds number is time dependent, with $0 \leq Re \leq 4200$.

Figure 3.9 compares the solution obtained with all the meshes reported in Table (3.4) both in terms of a global variable, the volume averaged arterial pressure, p_{avg}, defined as

$$p_{avg} = \frac{1}{\Omega}\int_{\Omega} p d\Omega, \tag{3.25}$$

and in terms of a local variable, the descending aorta cross-section pressure, p_{da}. We let the simulations run till transient effects are passed, $t^* \simeq 8 \cdot T$. For a more quantitative comparison, we computed the Weighted Absolute Percentage Error (WAPE) ϵ [63] with respect to the solution obtained with the finer mesh $2000k$:

$$\epsilon = \frac{100}{n}\sum_{i=1}^{n}\left|\frac{X_i - X_i^{2000k}}{\overline{X^{2000k}}}\right| \%, \tag{3.26}$$

where n is the number of sampling points, X_i is the solution related either meshes $230k$ and $415k$ at the i-th time step, X_i^{2000k} is the solution related to the mesh $2000k$ at the i-th time step and $\overline{X^{2000k}}$ is the time-averaged solution related to the mesh $2000k$. For p_{avg}, we obtained $\epsilon = 0.34\%$ for the mesh $230k$ and $\epsilon = 0.16\%$ for the mesh $415k$. On the other hand, for p_{da}, we obtained $\epsilon = 0.28\%$ for the mesh $230k$ and $\epsilon = 0.13\%$ for the mesh $415k$. Thus, hereinafter, in order to reduce the computational cost, we will refer to the solutions computed by using the mesh $230k$. Regarding the post-surgery configuration, we choose a mesh with a similar refinement, having $200k$ cells, $h_{min} = 6.3e-4$ and $h_{max} = 3.4e-3$.

mesh name	h_{min}	h_{max}	No. of cells
$230k$	5.8e-4	3e-3	228296
$415k$	5.6e-4	2.5e-3	414192
$2000k$	4.4e-4	1.5e-3	1993514

Table 3.4: Name, minimum diameter h_{min} , maximum diameter h_{max}, and number of cells for all the meshes used for the convergence study.

	Re
Pre-surgery	[0, 4200]
Post-surgery: test 1	1818
Post-surgery: test 2	1862
Post-surgery: test 3	1995
Post-surgery: test 4	2217

Table 3.5: Reynolds number Re for all the flow regimes under consideration.

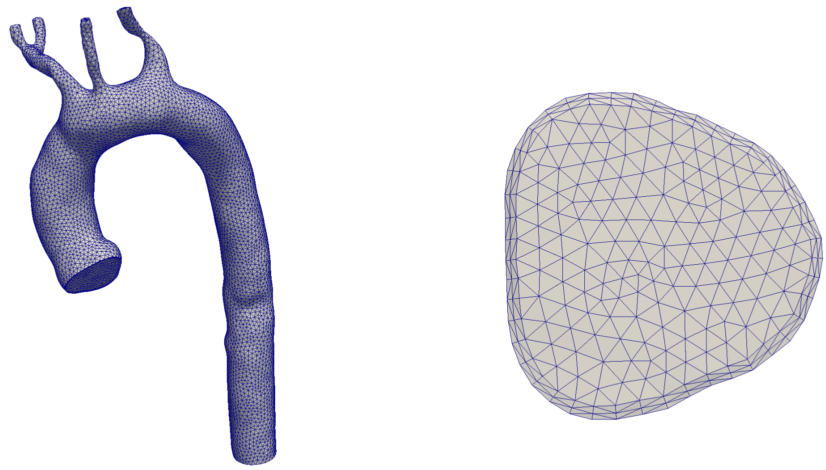

Figure 3.8: View of the mesh 230k: (left) aortic wall, (right) a section next to the aortic inlet.

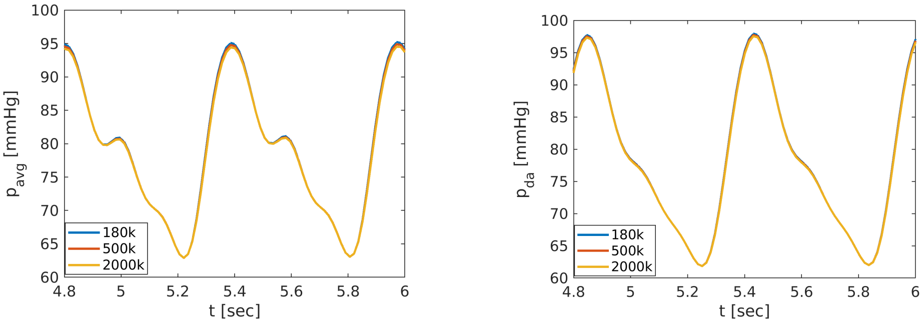

Figure 3.9: Pre-surgery configuration: time evolution on two cardiac cycles of the volume averaged arterial pressure p_{avg} as defined in (3.25) (left) and the pressure related to the descending aorta cross-section p_{da} (right) for the different meshes under consideration.

Pre-surgery configuration

The comparison between computational and experimental data is carried out in terms of systolic arterial pressure PAS, diastolic arterial pressure PAD and average arterial pressure PAM. Computational estimates of such quantities are evaluated by simulations in the following way:

$$PAS = \max_{t\in[0,T]} p_{avg}, \tag{3.27}$$

$$PAD = \min_{t\in[0,T]} p_{avg}, \tag{3.28}$$

$$PAM = \frac{1}{T}\int_0^T p_{avg} dt. \tag{3.29}$$

Figure 3.9 (left) shows the temporal evolution of p_{avg} (equation (3.25)). Table 3.6 reports both numerical and experimental data marked by the abbreviations *num* and *exp*, respectively. We observe that the agreement is very good, within 11.7% for PAS, 4% for PAD and, 2.4% for PAM. Figure 3.10 displays the TAWSS magnitude distribution. Since in this case experimental data are not available, we just provide rough indications in order to justify the patterns obtained. Basically, we observe that peak values of TAWSS are localized in regions where narrowing of cross section happens. On the other hand, regions characterized by lower TAWSS correspond to section enlargements. These results are expected by considering the classic findings for a straight cylindric vessel with steady Poiseuille flow. In this simplified case, $WSS \propto \dfrac{1}{d^3}$, where d is the pipe diameter. For biomedical experimental works that confirm such trend, the reader could see, e.g., [64, 65].

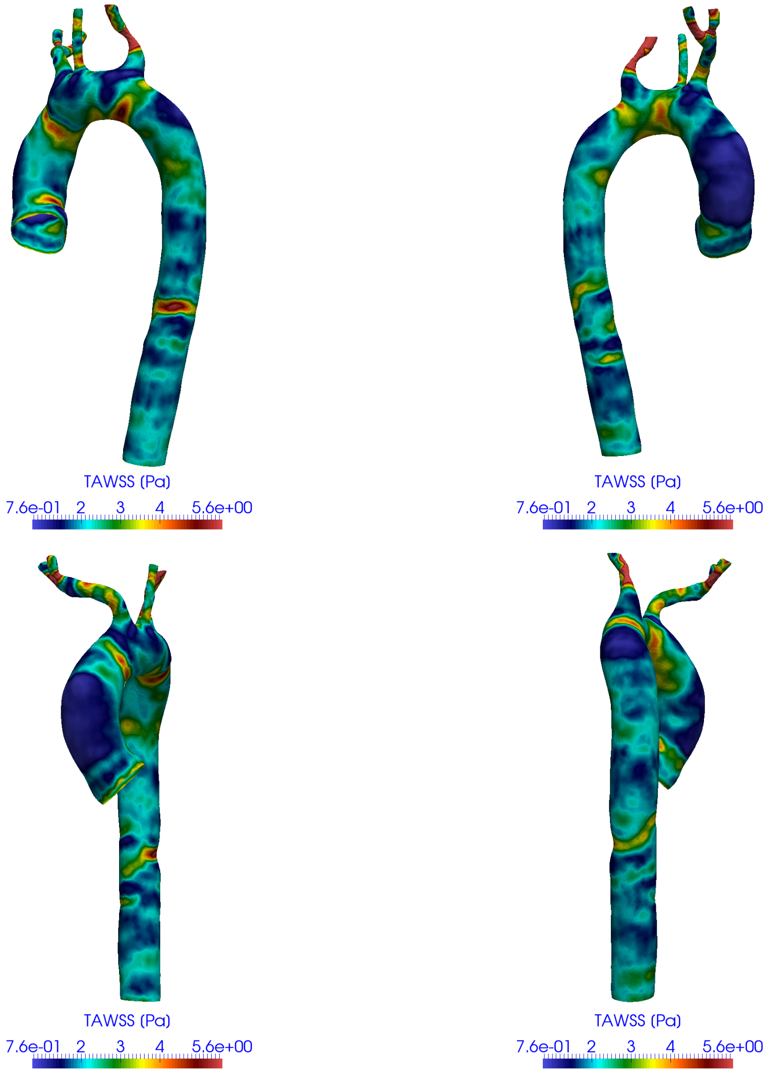

Figure 3.10: Pre-surgery configuration: TAWSS magnitude distribution on the entire wall of the model.

Figure 3.11 (left) depicts time averaged velocity streamlines. As expected, we note the generation of helical flow patterns in the aortic arch region (see, e.g. [66]).

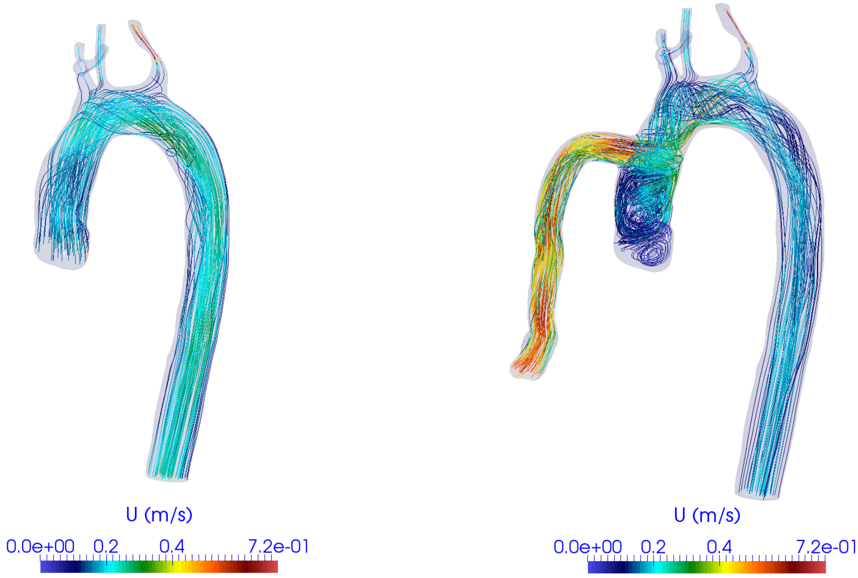

Figure 3.11: Velocity streamlines related to the pre-surgery configuration (left) and the post-surgery configuration for $PF = 4.1$ l/min and $\omega = 5400$ rpm (right).

PAS (exp/num) [mmHg]	*PAD (exp/num) [mmHg]*	*PAM (exp/num) [mmHg]*
108/95.4	66/63.4	78/79.9

Table 3.6: Pre-surgery configuration: comparison between computational and experimental data.

Post-surgery configuration

Unlike the pre-surgery case, in the post-surgery configuration, since the LVAD flow rate is continuous and not pulsatile, and the aortic valve is closed, the solution is steady in time. Therefore, the comparison between computational and experimental data is based on a value only, $PAM = PAD = PAS$. Table 3.7 reports both numerical (*num*) and experimental (*exp*) data for all the PF values considered. We observe that the agreement is excellent, within 1% in all the cases. Figures 4.6-4.9 show the WSS distribution for the three configurations investigated. As for the pre-surgery configuration, even in this case experimental data related to WSS are not available but it is possible to provide some interesting observations to be compared with previous works. In all the cases, we observe that there are high WSS, significantly greater than that obtained in the pre-surgery configuration, on the posterior region of the aortic arch, in front of the anastomosis. This high WSS zone is associated with the impingement of the jet from the cannula. This result is in agreement with those observed by [67, 68, 69]. Moreover we observe that elevated WSS also occur near the location of the outflow cannula, as found by [70, 71, 72, 73, 74, 75, 76]. On the contrary, on the most part of the aortic arch and descending aorta, very low WSS occurs. These patterns are critical from clinical points of view because highly heterogeneous WSS distribution coupled with the presence of a small region of the aortic arch exposed to high WSS could be associated to the development of atherosclerosis [77, 78]. Finally, we note that at increasing of PF from 4.1 to 5 l/min, the peak value of WSS moves from 12 to 15 Pa by following an almost linear trend. Figure 9 (right) displays the velocity streamlines for the Test 1. With respect to the pre-surgery configuration, we observe that in the ascending aorta, below the anastomosis location, retrograde flow and recirculation zone generate [79, 80, 70, 73, 81]. Moreover, the swirling flow in the aortic arch seems more intensive. In addition, we observe that velocity values in the outflow cannula are higher than those in aorta because of its small diameter.

PF [l/min]	PAM (exp/num) [mmHg]
4.1	78/78.6
4.2	90/90.6
4.5	100/100.7
5	83/82

Table 3.7: Post-surgery configuration: comparison between computational and experimental data.

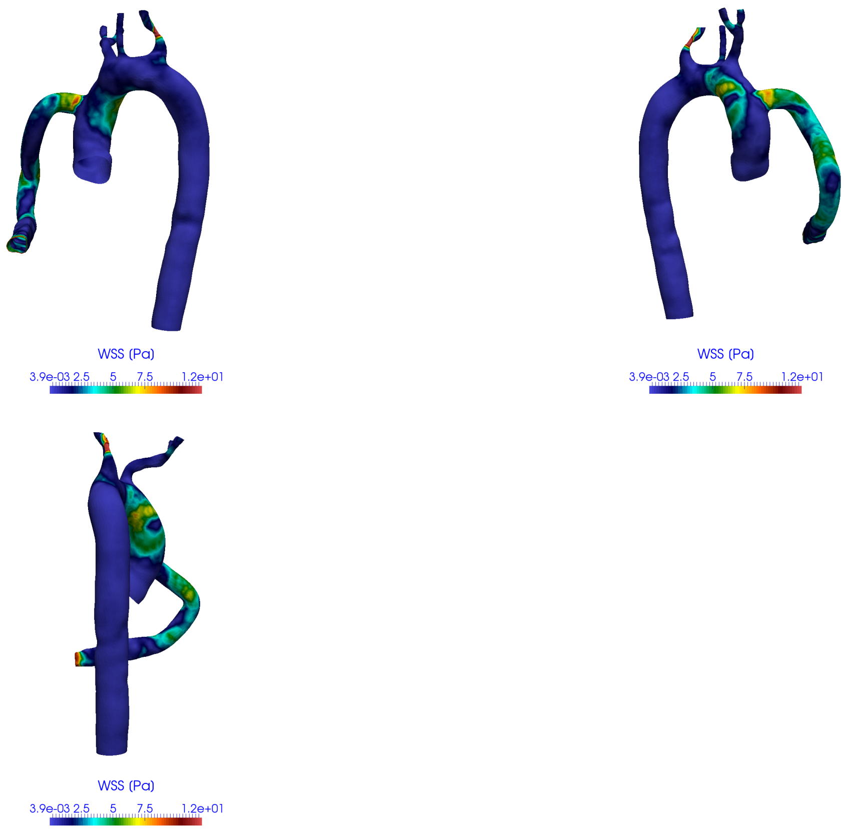

Figure 3.12: Post-surgery configuration: distribution of the WSS magnitude for $PF = 4.1$ l/min and $\omega = 5400$ rpm.

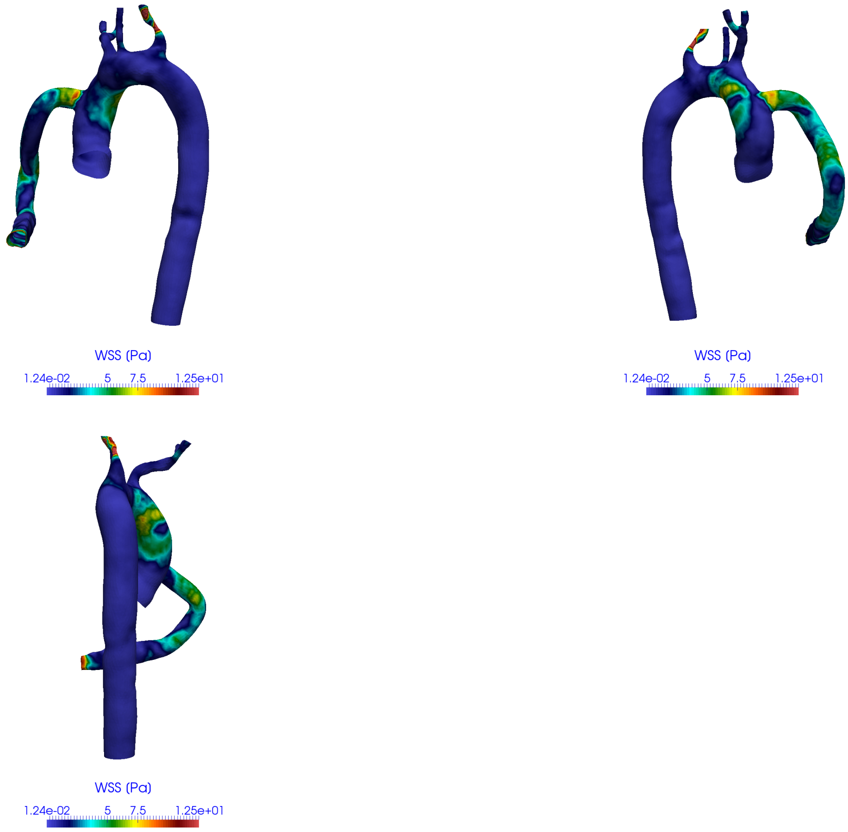

Figure 3.13: Post-surgery configuration: distribution of the WSS magnitude for PF = 4.2 l/min and ω = 5600 rpm.

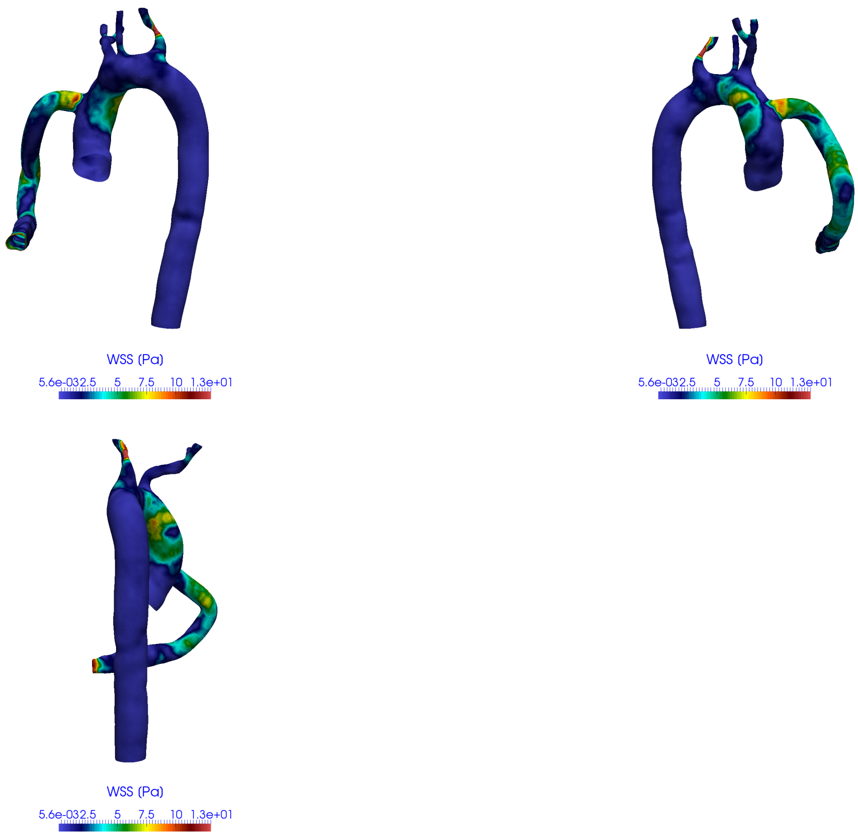

Figure 3.14: Post-surgery configuration: distribution of the WSS magnitude for PF = 4.5 l/min and ω = 6000 rpm.

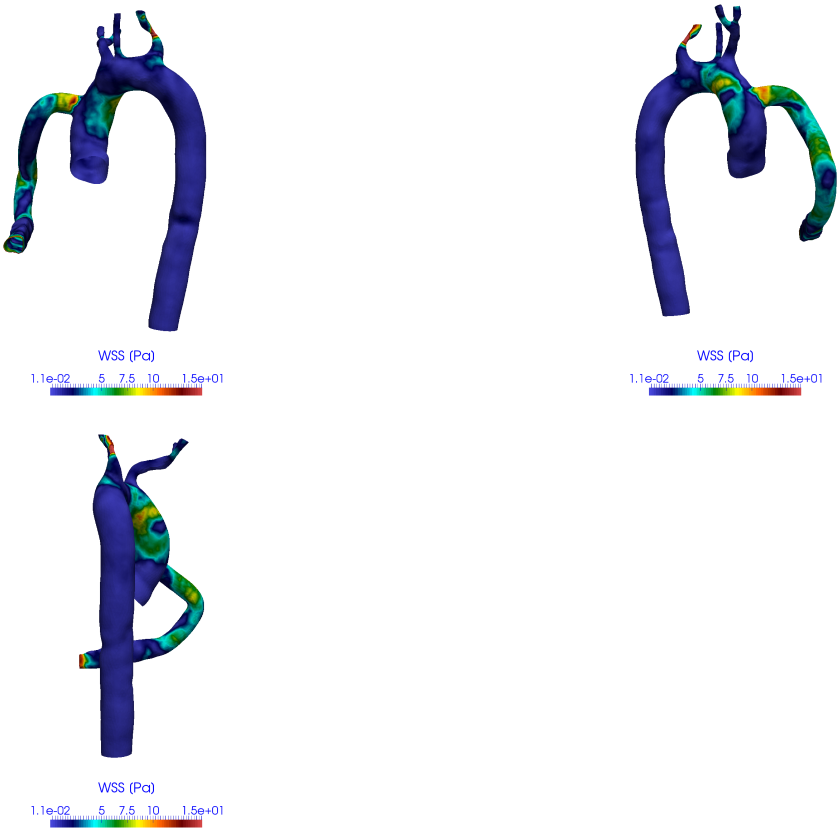

Figure 3.15: Post-surgery configuration: distribution of the WSS magnitude for $PF = 5$ l/min and $\omega = 5600$ rpm.

Chapter 4

Reduced Order Methods

Reduced Order Methods (ROMs) are a huge category techniques used to reduce the complexity of a mathematical model and consequently the computational cost required to obtain the numerical solution. The contexts in which this reduction is convenient are numerous in engineering.

The main idea behind ROM is that a generic problem, even very complex, has an intrinsic dimension much lower than the number of degrees of freedom of the discretized system[82, 83, 84]. To achieve this dimensionality reduction, a database of several solutions is firstly collected by solving the original high-order model for different physical and/or geometrical parameters (offline phase).

In this chapter, we discuss in more detail Reduced Basis ROMs and the technique that will be used extensively during this work, i.e. Proper Orthogonal Decomposition (POD), with the PODI (POD with interpolation) variant. For this purpose, we will briefly recall the theory of Singular Value Decomposition (SVD).

We introduce the notion of the solution manifold, that is the set of all possible solutions of our parametric problem under the variation of the parameter; then, all the solutions are combined to build the space onto which we can accurately project the solution manifold and efficiently compute the solutions for the new parameters (online phase).

The final goal of RB methods is to approximate any element of this manifold using a low number of basis functions, or modes, that form what we call the reduced basis.

4.1 Reduced Basis ROMs (RB-ROMs)

We begin with a formal definition of a system of parametric PDEs:

$$\text{find } u(\mu) \in \mathbf{Y} \text{ s.t.: } a(u(\mu), w; \mu) = F(w; \mu) \ \forall w \in \mathbf{Y}, \tag{4.1}$$

where $\mu \in \mathbf{P}$ is the parameter and $u(\mu) \in \mathbf{Y}$ is the **exact solution** of the problem (4.1).

At this point we give the definition of the *solution manifold*, that is the set that contains all the possible solutions of the parametric problem under the variation of the parameter:

$$\mathbb{M} = \{u(\mu),\ \mu \in \mathbf{P}\}. \tag{4.2}$$

In most situations the exact solution is not reachable analytically so it is approximated numerically. The so-called *truth solution* can be obtained using, for example, the different Full Order Model techniques described in the previous sections. We call the truth solution of our problem with $u^{\mathcal{N}}$, where $\mathcal{N}$ is the number of degrees of freedom associated with it; if $\mathcal{N}$ has a big value, it implies a high dimension of the linear system resulting from the application of the FOM and consequently a high computational cost. Starting from the (4.1), the problem related to the trurh solution is:

$$\text{find } u^{\mathcal{N}}(\mu) \in \mathbf{Y}^{\mathcal{N}} \text{ s.t.: } a(u^{\mathcal{N}}(\mu), w; \mu) = F(w; \mu) \quad \forall w \in \mathbf{Y}^{\mathcal{N}}, \tag{4.3}$$

where $\mathbf{Y}^{\mathcal{N}}$ is a finite dimensional subspace of $\mathbf{Y}$ of dimension $\mathcal{N}$.
The manifold is then defined by:

$$\mathbb{M}^{\mathcal{N}} = \{u^{\mathcal{N}}(\mu),\ \mu \in \mathbf{P}\}. \tag{4.4}$$

The main task of Reduce Basis methods is to approximate any element of $\mathbb{M}^{\mathcal{N}}$ using a low number of basis functions, (also colled *modes*), $\{\chi_i(x)\}_{i=1}^{N}$, that form what we call the reduced basis. These functions are defined over the computational domain and are obtained using some pre-computed truth solutions for particular parameter values as we will see subsequently. The *reduced solution* $u_N^{\mathcal{N}} \simeq u^{\mathcal{N}}$ is composed by a suitable linear combination of these modes:

$$u_N^{\mathcal{N}}(\mu) = \sum_{i=1}^{N} \xi_i(\mu)\chi_i(x). \tag{4.5}$$

At this point we are ready to write the reduced version of the (4.3):

$$\text{find } u_N^{\mathcal{N}}(\mu) \in \mathbf{Y}_N^{\mathcal{N}} \text{ s.t.: } a(u_N^{\mathcal{N}}(\mu), w; \mu) = F(w; \mu) \quad \forall w \in \mathbf{Y}_N^{\mathcal{N}}, \tag{4.6}$$

where $\mathbf{Y}_N^{\mathcal{N}} = span\big(\{\chi_i(x)\}_{i=1}^{N}\big)$. Clearly for the RB approximation to be useful, the degrees of freedom associated with the RB approximation (N) should be much less than the degrees of freedom associated with the truth solution ($\mathcal{N}$), so N $\ll$ $\mathcal{N}$. This approach in which the original equations (4.3) are projected onto the reduced basis space, giving the (4.6) is called *intrusive approach* (see [31], [30]), however in this thesis we will work with a *non-intrusive approach* as we will describe in the next sections.

4.2 Proper Orthogonal Decomposition (POD)

Proper orthogonal decomposition (POD) is a technique widely used within the reduced order modeling (ROM) framework for the study of parametric problems. We will call a possible outcome of our system $\mathbf{z}$ a snapshot and denote with m its dimensionality ($\mathbf{z} \in \mathbb{R}^m$). We will then denote with n the number of snapshots collected in the offline phase. POD allows to extract, from a set of high-dimensional snapshots, the basis minimizing the error between the original snapshots and their orthogonal projection. The original snapshots are projected onto the POD space in order to reduce their dimensionality. POD consists of a Singular Value Decomposition applied to a set of high fidelity solutions. Let us define a *snapshots' matrix* $\mathbf{Z} \in \mathbb{R}^{m \times n}$:

$$\mathbf{Z} = \begin{bmatrix} | & | & & | \\ \mathbf{z}_1 & \mathbf{z}_2 & \dots & \mathbf{z}_n \\ | & | & & | \end{bmatrix}. \tag{4.7}$$

The matrix $\mathbf{Z}$ will have, in general, a rank $d \leq \min(m, n)$ but, we could restrict our analysis to the case $d = n < m$, in fact the $n < m$ condition is guaranteed by the fact that we are treating really high dimensional snapshots, in which $n \ll m$; for example, we may have values of m with an order of magnitude near to the hundreds of thousands, while the number of snapshots n will be of the order of hundreds.

The condition $d = n$ is, instead, guaranteed by the fact that we are dealing with output of a very complex system and it is pretty impossible that the snapshots matrix is composed by snapshots linearly dependent. In other words it's very unlikey that the snapshots matrix will not be of full rank.

We call l the number of POD modes that will be used to construct the law-rank approximation, with $l < n < m$.

At this point we have to recall the following theorem that explain us the Singular Value Decomposition:

Theorem 1. ***(SVD)*** *Given* $\mathbf{Z} \in \mathbb{R}^{m \times n}$ *of rank* $d = n < m$*:*

- $\exists\ \sigma_1 \geq \sigma_2 \geq ... \geq \sigma_n > 0$ *(singular values);*
- $\exists\ \mathbf{\Psi} \in \mathbb{R}^{m \times m}$ *orthogonal with columns* $\{\psi_i\}_{i=1}^m$ *(left singular vectors);*
- $\exists\ \mathbf{\Phi} \in \mathbb{R}^{n \times n}$ *orthogonal with columns* $\{\phi_i\}_{i=1}^n$ *(right singular vectors);*

with $\mathbf{Z} = \mathbf{\Psi\Sigma\Phi}^T$ *and* $\mathbf{\Sigma} = \begin{pmatrix} \sigma_1 & & \\ & \ddots & \\ & & \sigma_n \\ & & \\ & & \end{pmatrix} \in \mathbb{R}^{m \times n}$.

The following properties hold:

1. $\mathbf{Z}\phi_i = \sigma_i \psi_i,\ i = 1, ..., n;$
2. $\mathbf{Z}^T \psi_i = \sigma_i \phi_i,\ i = 1, ..., m;$
3. ψ_i *is an eigenvector of* $\mathbf{ZZ}^T$ *with eigenvalue* σ_i^2 *(for* $i = 1, ..., m$*);*
4. ϕ_i *is an eigenvector of* $\mathbf{Z}^T\mathbf{Z}$ *with eigenvalue* σ_i^2 *(for* $i = 1, ..., n$*).*

The third property reported in the theorem states that to obtain the matrix $\mathbf{\Psi}$ one could solve an eigenvalue problem on $\mathbf{ZZ}^T$, that we can interpret as a covariance matrix on the snapshots. This observation suggests that in some sense the left eigenvectors are directions that maximize the variance of the space spanned by these vectors.

To make the last assertion more precise, let us proceed with the formal definition of the POD basis:

Theorem 2. ***(POD basis)*** *Given* $\mathbf{Z} \in \mathbb{R}^{m \times n}$ *of rank* $d = n < m$, $\{\chi_i\}_{i=1}^l$, *for* $l \in \{1, .., n\}$ *is the POD basis of* $\mathbf{Z}$ *if and only if it is a solution of:*

$$\max_{\tilde{\psi}_1, \tilde{\psi}_2, .. \tilde{\psi}_l} \sum_{i=1}^{l} \sum_{j=1}^{n} | < \mathbf{z}_j, \tilde{\psi}_i >_{\mathbb{R}^m} |^2 \quad s.t. < \tilde{\psi}_i, \tilde{\psi}_i >_{\mathbb{R}^m} = \delta_{i,j}, \quad for\ 1 \leq i, j \leq n. \tag{4.8}$$

The theorem 2 states that the POD basis is the one that maximizes the similarity between the snapshots matrix and its elements, considering the constraint of orthonormality. So once we obtain the l-rank POD basis, we have the set of dimension l capable of optimally express the variance in the snapshots. At this point we need a link between POD and SVD, and this link is stated by the following theorem, that can be proven using Lagrangian penalization techniques (see [29]):

Theorem 3. *Given $\mathbf{Z} \in \mathbb{R}^{m\times n}$ of rank $d = n < m$, its l-rank POD basis is given by the set of the first l left singular vectors $\{\psi_i\}_{i=1}^{l}$ Moreover, we have:*

$$\max_{\tilde{\psi}_1,\tilde{\psi}_2,..\tilde{\psi}_l} \sum_{i=1}^{l}\sum_{j=1}^{n} | < \mathbf{z}_j, \tilde{\psi}_i >_{\mathbb{R}^m} |^2 = \sum_{i=1}^{l} \sigma_i^2. \tag{4.9}$$

4.3 Proper Orthogonal Decomposition with Interpolation (PODI)

The data-driven approach here used is based only on data and does not require knowledge about the governing equations that describe the system. It is also non-intrusive, i.e. no modification of the simulation software is carried out. On the other hand, there are works that use non-intrusive methods that are not data-driven (see, e.g., [28]). The original snapshots are projected onto the POD space in order to reduce their dimensionality. A considerable difference, however, is that while in intrusive POD we need to rely upon an open-source software to compute the truth solutions, since in the online phase we will need to have access to the source code in order to project the equations. In the PODI approach instead we don't need to do this, and we can use commercial software or even experimental data to train our model.

At this point the solution manifold is approximated using an *interpolation* technique. Several examples of applications based on this so-called POD with interpolation (PODI) [27] techique can be found in literature, in a wide range of contexts: naval engineering problem [26, 25, 21], automotive [20, 17], aeronautics [16]. We also cite [15] where a coupling with isogeometric analysis is performed.

We recall here that the assumption of RB-ROMs is that the truth solution of our problem $u^{\mathcal{N}}$ can be approximated by the reduced solution $u_N^{\mathcal{N}}$ composed by linear combination of spatial modes $\chi_i(x)$ multiplied by coefficients $\xi_i(\mu)$, that is:

$$u^{\mathcal{N}}(\mu) \approx u_N^{\mathcal{N}}(\mu) = \sum_{i=1}^{N} \xi_i(\mu)\chi_i(x). \tag{4.10}$$

In PODI then we define an interpolator considering with a function that associates the value of the parameter μ to the modal coefficients of the related solution $\{\xi_i(\mu)\}_{i=1}^{N}$. This multi-dimensional interpolator is (using a machine learning language) *trained* using the data coming from the snapshots matrix, in which we know both the parameter values and the modes coefficients are, and is then used to infer the value of the coefficients associated with new parameters. The values of the coefficients are finally used to reconstruct the approximated truth solution using (4.10).

As we said before this approach is totally data-driven and is independent both on the equations and on the physics of the problem.

Regarding the technical implementation of the PODI method, we use the Python package called EZyRB [13].

4.4 Simulation Results

In this section we will show the results obtained by simulations by applying the ROMs theory described in the previous chapter. Clearly from now on we will work with *Post-surgery configuration* which is the configuration of interest in this thesis.

To train the ROM, the values of the LVAD flow rate, PF, are chosen using an equispaced distribution inside the range $PF \in [3, 5]$ that covers typical clinical values. Two sampling cases were considered. In the first case, we have 21 snapshots, and in the second one, 11 snapshots. Thus, the snapshots are collected every 0.1 in the first case and 0.2 in the latter one. For all the simulations, we use resistances and capacitances of Test 1 (see Tables 2.6, 2.7, 2.9). By assuming that we vary PF, and consequently ω, at a given $\Delta P = 75$ (see Table 2.5) and using the analytical fit 11, we obtain that the range $PF \in [3, 5]$ corresponds to $\omega \in [5076, 5720]$. Two new values of the $PF(\omega)$ in which the ROM has not been trained but which belongs to the range of the training space, $PF = 3.45$ ($\omega = 5200$) and $PF = 4.35$ ($\omega = 5484$), are used to evaluate the performance of the parametrized ROM. POD modes and coefficients are computed as explained in Section 5.2. Figure 4.1 shows the cumulative energy of the eigenvalues for pressure p, wall shear stress WSS, and velocity components, u_x, u_y and u_z. In order to retain the 99.9% of the system's energy, when we consider 21 snapshots, 1 mode for p, 14 for WSS, 16 for u_x, u_y and u_z are selected. On the other hand, when 11 snapshots are taken into account, 1 mode for p, 9 for WSS, 8 for u_x, u_y and u_z are selected. Moreover, to provide some quantitative results, the relative error in the L^2-norm, calculated as:

$$E_X = 100\frac{||X_{FOM} - X_{ROM}||_{L^2(\Omega)}}{||X_{FOM}||_{L^2(\Omega)}}\%. \tag{4.11}$$

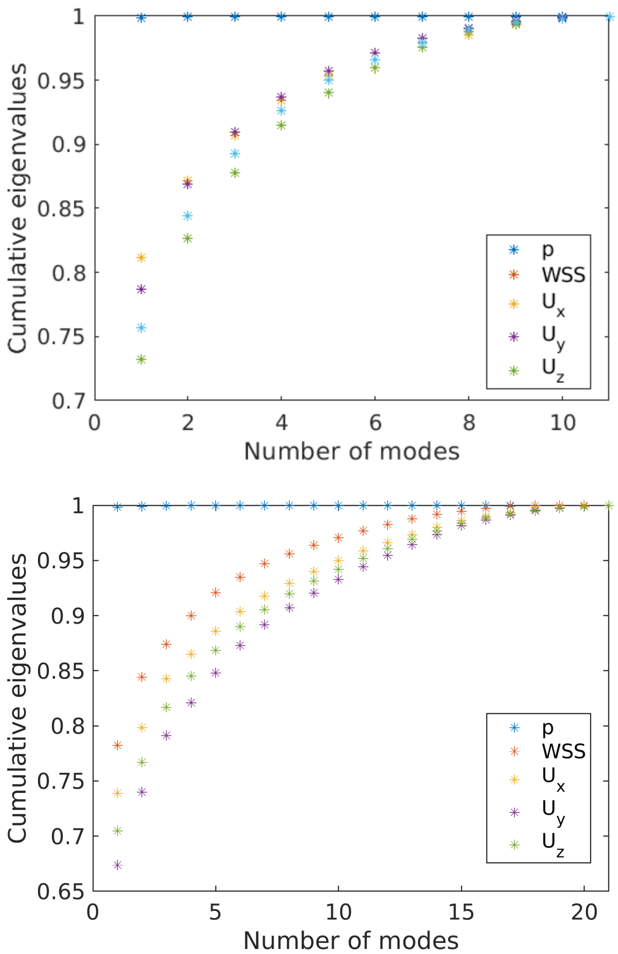

Figure 4.1: Cumulative energy of the eigenvalues for pressure p, wall shear stress WSS, and velocity components, u_x, u_y and u_z. The sampling frequency of the eigenvalues is 0.2 (left) and 0.1 (right),

where X_{FOM} is the value of a particular field in the FOM model, and X_{ROM} the one that is calculated using the ROM, is considered. In Tables 4.1 and 4.2, one could observe that the differences between the two spaces are minimal, for both the values of PF considered. Therefore, hereinafter results will be based on the database of 11 snapshots.

	p	WSS	u_x	u_y	u_z
E_X (21 snapshots)	0.1%	4.1%	5.6%	7.9%	6.2%
E_X (11 snapshots)	0.2%	4.1%	5%	7.8%	5.8%

Table 4.1: L^2 norm relative errors for pressure p, wall shear stress WSS, and velocity components, u_x, u_y and u_z, to varying of the number of snapshots collected for $PF = 3.45$ l/min.

	p	WSS	u_x	u_y	u_z
E_X (21 snapshots)	0.2%	9.6%	10.7%	14.5%	10.5%
E_X (11 snapshots)	0.5%	7.2%	9.7%	13.5%	9.3%

Table 4.2: L^2 norm relative errors for pressure p, wall shear stress WSS, and velocity components, u_x, u_y and u_z, to varying of the number of snapshots collected for $PF = 4.35$ l/min.

Figure 4.2 and 4.3 display a comparison between FOM and ROM for p and WSS fields, for both $PF(\omega)$ values under consideration. The comparison indicates that the ROM is able to provide a good reconstruction for both variables. Figure 4.4 displays the velocity streamlines obtained both with FOM and ROM, and for both $PF(\omega)$ values under consideration. In order to further investigate the flow field, in Figure 4.5 a comparison between FOM and ROM for the velocity field related to a section of the ascending aorta next to the anastomosis location is showed. As observed for p and WSS fields, the ROM also performs well for the velocity.

The CPU time of the FOM model is 9600s and the one of the ROM is 40s. This corresponds to a speed-up of $\simeq 240$, that demonstrates the fact that it is possible to use the ROM in the place of the FOM in order to obtain accurate simulations with a significant reduction of the computational cost.

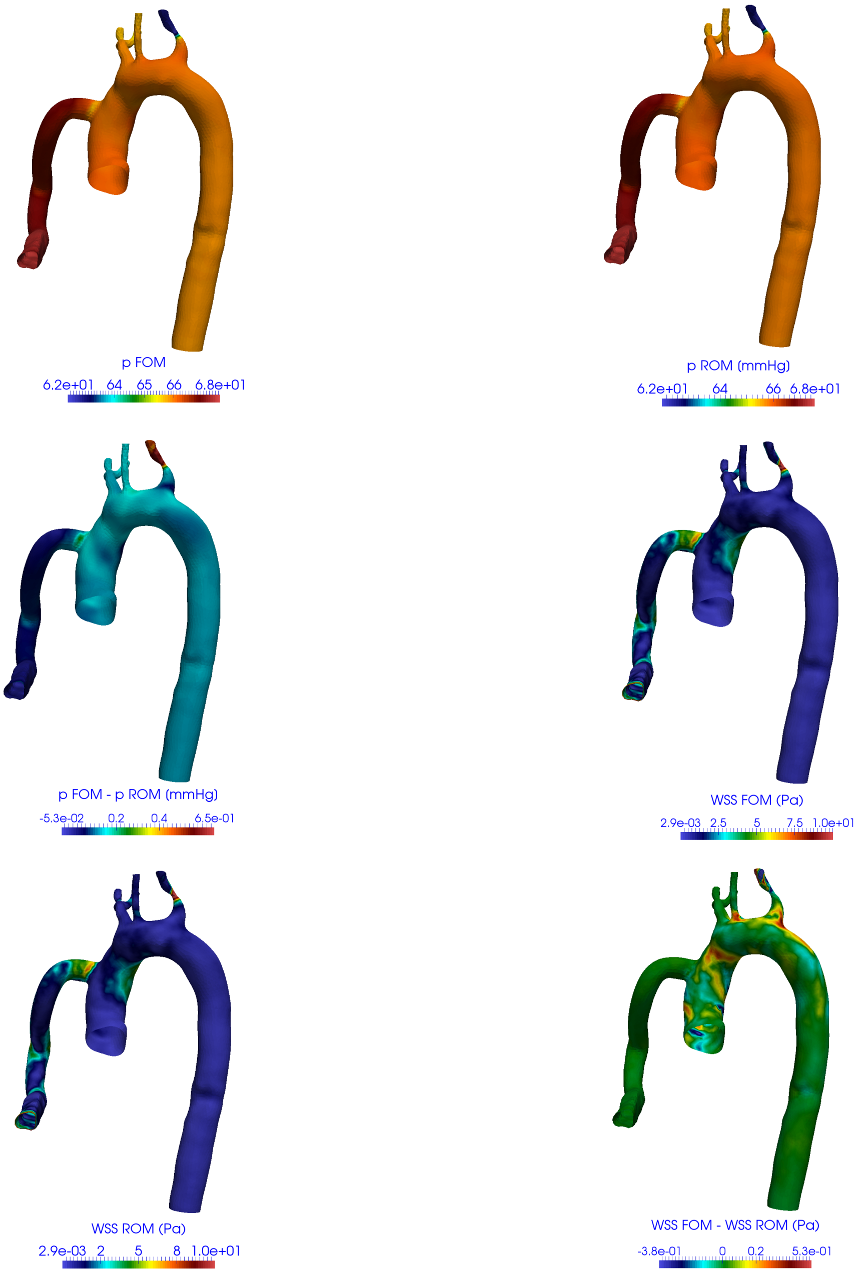

Figure 4.2: Comparison of the FOM/ROM pressure (1st row) and WSS (2nd row) at $PF = 3.45$ ($\omega = 5200$).

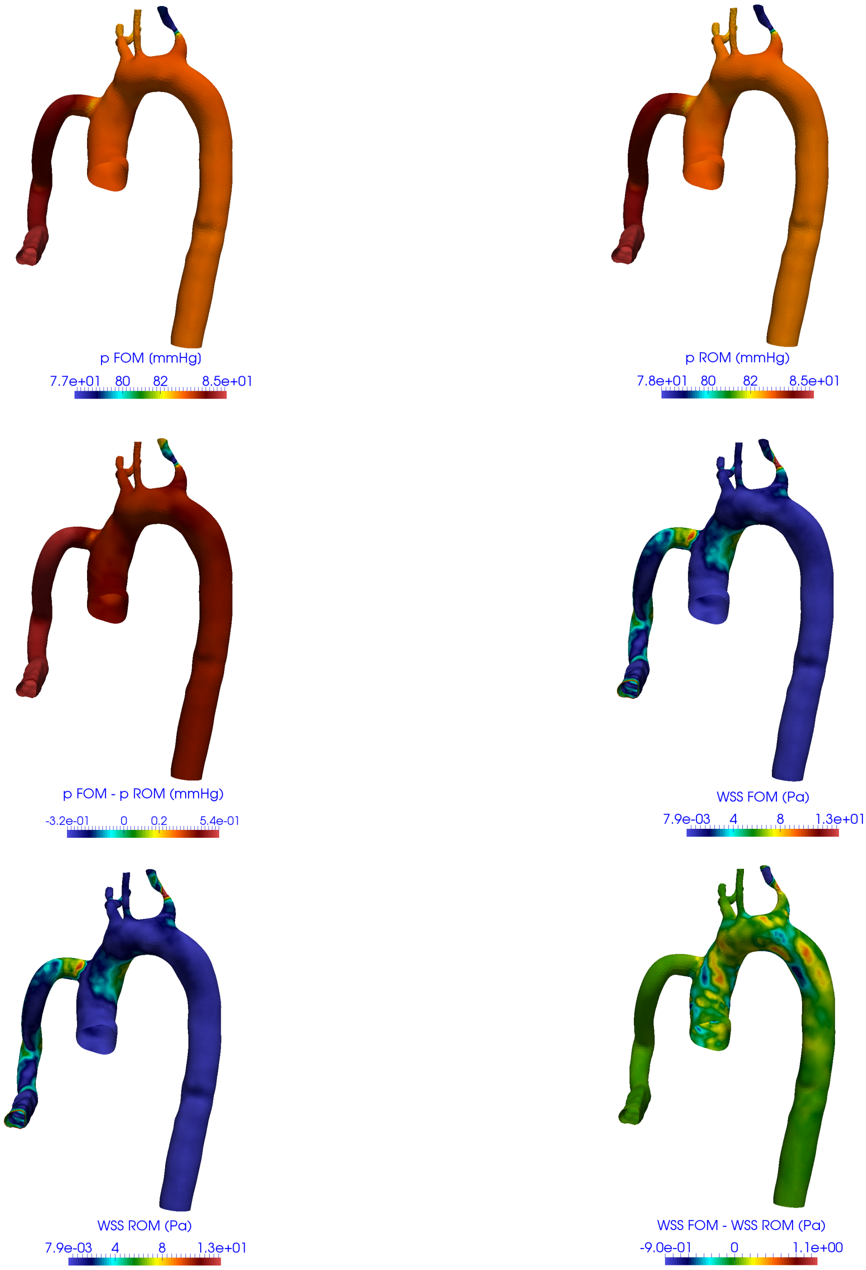

Figure 4.3: Comparison of the FOM/ROM pressure (1st row) and WSS (2nd row) at $PF = 4.35$ ($\omega = 5484$).

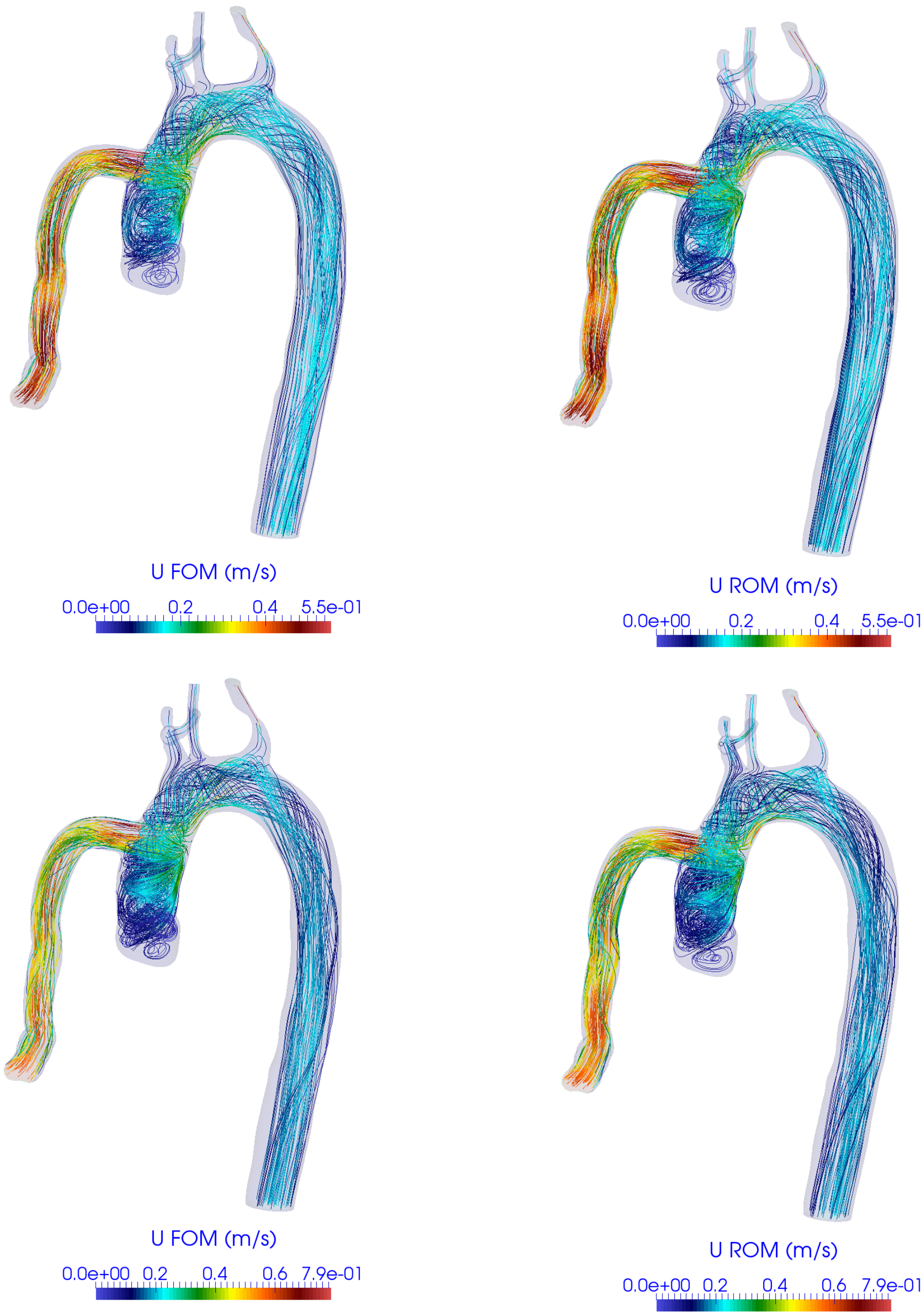

Figure 4.4: Comparison of the FOM/ROM velocity streamlines at $PF = 3.45$ ($\omega = 5200$) (1st row) and $PF = 4.35$ ($\omega = 5484$) (2nd row).

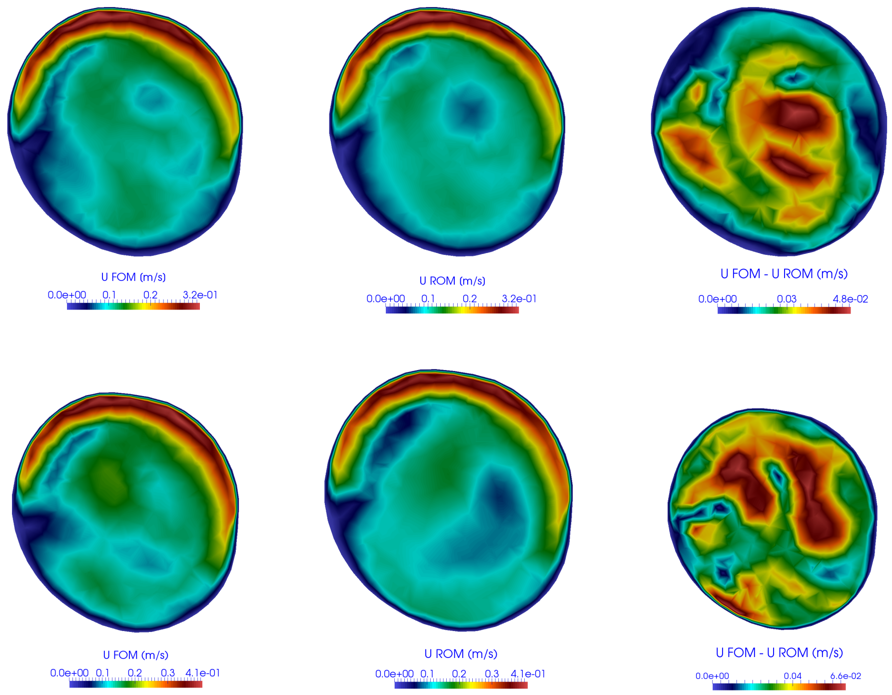

Figure 4.5: Comparison of the FOM/ROM velocity field related to a section of the ascending aorta next to the anastomosis location at $PF = 3.45$ ($\omega = 5200$) (1st row) and $PF = 4.35$ ($\omega = 5484$) (2nd row).

Chapter 5

Conclusion and Perspectives

In this work, a parametrized non-intrusive ROM using PODI method is used for the investigation of patient specific aortic blood flow in presence of a LVAD device. The goal of this Master Thesis is to investigate the phenomena that characterize the aortic blood flow after the surgical introduction of a left ventricular assist device (LVAD) by using a data-driven analysis. The FOM is represented by the incompressible Navier-Stokes equations. About the space discretization, both FEM and FV have been investigated. We have showed that they provide comparable results. Outlet boundary conditions have been enforced by using three-element Windkessel models. CT images of a patient are considered for the reconstruction of the geometry as well as RCH and ECHO data are exploit for the individualisation of the three-element Windkessel models coefficients used to enforce boundary conditions. Therefore, a complete patient-specific framework is presented. In order to showcase the features of our approach, we have successfully validated the FOM both for pre-surgery and post-surgery configuration by comparing numerical and experimental data. Then, the ROM developed is used to carry out a parametric study with respect to the LVAD flow rate. We show that the ROM provides accurate solutions with a significant reduction of the computational cost, up to at least two orders of magnitudes. We want to emphasize the flexibility given by the data-driven approach that allows us to consider various different possibilities for the generation of the FOM snapshots, for example considering commercial CFD software or experimental data.

Finally, we want to highlight some of the future perspectives of this work. We are going to investigate the influence of the LVAD device on the left and right ventricle flow patterns as well as their interaction. We are also interested in efficiently handling geometrical parametrization (e.g. in order to consider different anastomosis angles, or different designs of the outflow cannula) in the context of patient-specific geometries, extending e.g. the work carried out in [10] to different applications and different model reduction techniques.

The final objective of the scientific research project in which this thesis is inserted is to provide to people working in biomedical environment digital tools, capable of developing a final package of operations that makes the calculation usable and efficient. For example, enabling a surgeon in the operating room to obtain very useful indicators related to a determined operation by having access from a tablet to the billions of calculations made by a supercomputer.

In general, the idea is to have a code available that allows you to consult, in real time, a database of calculations and solutions. More specifically, the idea consists in preparing increasingly complex simulations on supercomputers, but making them parametric and projecting them, thanks to the existence of simulation databases, towards digital instruments; at this point we continue by breaking down the calculation operations into various steps so that the supercomputer can assemble the various pieces which are then processed by immediate numerical methods, which are based on some studied and certified algorithms that have allowed, as mentioned above, to bring the so-called real-time calculation on devices accessible to everyone. Returning to the medical field of application, the clinical data and patient information, anonymously, provided by hospitals, such as the CT images and other data that we used in this work, are inserted in the memory that the supercomputer then elaborates creating in this way computational simulation databases: this phase is called *offline phase*, subsequently this database can be used by doctors by means of very simple devices (the aforementioned tablets) thanks to apps and therefore in no time (*online phase*); so an extraordinary result would be obtained: the work of weeks-months would become accessible in seconds.

In the future, doctors and surgeons could be able to reproduce a surgical engineering design in which, using simulations to create virtual surgery scenarios or other options, they can thus instruct their team before operating.

The clinical data, which at this point becomes a simulation, is the starting point for creating a model capable of describing all the cardiovascular functioning of a patient, in fact, as mentioned above, there is a direct correlation between the geometry of the cardiovascular system and the possible occurrence of certain diseases. In this way it will therefore be very simple to act and work in a *patient specific* way, i. e., customizing the precise anatomy, physiology, or health care needs of one single person.

Another very important point to consider is given by the predictive possibilities that can be had by having a rich database of computational simulations available, in fact with a rich database through machine learning techniques can be an option to maintain the equation-free nature of our approach and at same time increase the accuracy of the approximated output of interest. Moreover, with the big computational reduction, we can adopt this methods in order to build a digital twin of complex system, allowing the generation of virtual model that replicate in *real-time* the behaviour of the original system.

For example, we could study the probabilities of evolution of a certain condition of the patient towards pathologies such as stroke or heart attacks, so the usefulness of this work would be huge even outside the operating room in fact, unfortunately, nowadays, cardiovascular diseases are the main cause of death in developed countries, in particulare we are having that heart failure is a globally increasing health problem.

By now it can be said that supercomputing represents a measure of the industrial development of a country; in Italy there are some valuable projects in this field such as the supercomputer *Leonardo* of the Cineca, Bologna. In recent years the development of industry 4.0, augmented reality, the management of big data that improve mathematical models are increasing the importance of supercomputers.

Bibliografy

[1] K. Aaronson, M. Slaughter, L. Miller, E. McGee, W. Cotts, M. Acker, M. Jessup, I. Gregoric, P. Loyalka, O. Frazier,296 V. Jeevanandam, A. Anderson, R. Kormos, J. Teuteberg, W. Levy, D. Naftel, R. Bittman, F. Pagani, D. Hathaway, and297 S. Boyce, *Heartware ventricular assist device (hvad) bridge to transplant advance trial investigators. Use of an intrapericardial, continuous-flow, centrifugal pump in patients awaiting heart transplantation*, Circulation, vol. 125, pp. 3191-3200, 2012.

[2] L. C. Evans , *Partial Differential Equations.* American Mathematical Society, vol. 19, 1998.

[3] B. Liu, J. Zheng, R. Bach, D. Tang, *Influence of model boundary conditions on blood flow patterns in a patient specific stenotic right coronary artery*, BioMedical Engineering OnLine, pp, 1-14, 2015.

[4] I. E. Vignon-Clementel, C. A. Figueroa, K. E. Jansen, C. A. Taylor, *Outflow boundary conditions for three-dimensional finite element modeling of blood flow and pressure in arteries*, Computer Methods in Applied Mechanics and Engineering, vol. 195, pp. 3776-3796, 2006.

[5] M. Neidlin, C. Corsini, S. J. Sonntag,*Hemodynamic analysis of outflow grafting positions of a ventricular assist device using closed-loop multiscale CFD simulations*, Journal of biomechanics, vol. 49, pp. 2718-2725, 2016.

[6] L. Formaggia, A. Quarteroni, A. Veneziani, *Cardiovascular Mathematics: Modeling and simulation of the circulatory system*, MS&A, Springer Publishing, 2009.

[7] M. Anand, KR. Rajagopal, *A Shear-Thinning Viscoelastic Fluid Model For Describing The Fow Of Blood*, vol. 4, pp. 59-68, 2 2004.

[8] D. J. Tritton, *Physical fluid dynamics*, Springer Science and Business Media, 2012.

[9] R. Torii, M. Oshima, T. Kobayashi, K. Takagi, E. T. Tayfun, *Computer modeling of cardiovascular fluid–structure interactions with the deforming-spatial-domain/stabilized space–time formulation*, vol. 195, pp. 1885-1895, 16, 2006.

[10] F. Ballarin, E. Faggiano, A. Manzoni, A. Quarteroni, G. Rozza, S. Ippolito, C. Antona, and R. Scrofani, *Numerical modeling of hemodynamics scenarios of patient-specific coronary artery bypass grafts*, Biomechanics and Modeling in Mechanobiology, vol. 16, pp. 1373-1399, 4 2017.

[11] A. Quarteroni, *Modellistica numerica per problemi differenziali*, Springer Publishing, 2016.

[12] H. Brezis, *Functional Analysis, Sobolev Spaces and Partial Differential Equations*, Springer Publishing, 2011.

[13] N. Demo, M. Tezzele, and G. Rozza, *EZyRB: Easy reduced basis method*, Journal of Open Source Software, vol. 3, pp. 661, 2018.

[14] C. H. Chan, M. Czubak, *Remarks on the weak formulation of the Navier–Stokes equations on the 2D hyperbolic space*, Annales de l'Institut Henri Poincare (C) Non-Linear Analysis, vol.33, pp. 655-698, 3 2016.

[15] D. Forti and G. Rozza, *Efficient geometrical parametrisation techniques of interfaces for reduced-order modelling: application to fluid–structure interaction coupling problems*, International Journal of Computational Fluid Dynamics, vol. 28, 2014.

[16] M. Ripepi, M. Verveld, N. Karcher, T. Franz, M. Abu-Zurayk, S. Gortz, and T. Kier, *Reduced-order models for aerodynamic applications, loads and mdo*, CEAS Aeronautical Journal, vol. 9, 2018.

[17] V. Dolci and R. Arina, *Proper orthogonal decomposition as surrogate model for aerodynamic optimization*, International Journal of Aerospace Engineering 2016, vol. 2016, pp. 1–15.

[18] L. Catabriga, A. L. G. A. and T. E. Tezduyar, *Compressible Flow SUPG Stabilization Parameters Computed from Degree-of-freedom Submatrices*, Computational Mechanics, vol.38, pp. 334-343, 2006.

[19] J. E. Akin and T. E. Tezduyar, *Calculation of the advective limit of the SUPG stabilization parameter for linear and higher-order elements*, Computer Methods in Applied Mechanics and Engineering, vol. 193, pp. 1909-1922, 2004.

[20] F. Salmoiraghi, A. Scardigli, H. Telib, and G. Rozza, *Free-form deformation, mesh morphing and reduced-order methods: enablers for efficient aerodynamic shape optimisation*, International Journal of Computational Fluid Dynamics, vol. 32, pp. 233-247, 4-5 2018.

[21] N. Demo, M. Tezzele, and G. Rozza, *A non-intrusive approach for the reconstruction of POD modal coefficients through active subspaces*, Comptes Rendus Mecanique, vol. 347, pp. 873-881, 11 2019.

[22] SimVascular solvers. Avaiable at **https://simvascular.github.io/docsFlowSolver.html# solverconfiguration**.

[23] V. Girault and P. A. Raviart, *Finite element approximation of the Navier-Stokes equations*, Springer-Verlag, vol. 749, pp. 208-290, 1979.

[24] H. G. Weller, G. Tabor, H. Jasak, and C. Fureby, *A tensorial approach to computational continuum mechanics using object-oriented techniques*, Computers in physics, vol. 12, pp. 620–631, 6 1988.

[25] N. Demo, M. Tezzele, A. Mola, and G. Rozza, *An efficient shape parametrisation by free-form deformation enhanced by active subspace for hull hydrodynamic ship design problems in open source environment*, The 28th International Ocean and Polar Engineering Conference, volume 3, pp. 565–572, 2018.

[26] N. Demo, M. Tezzele, G. Gustin, G. Lavini, and G. Rozza, *Shape optimization by means of proper orthogonal decomposition and dynamic mode*

decomposition, Technology and Science for the Ships of the Future: Proceedings of NAV 2018: 19th International Conference on Ship & Maritime Research, IOS Press, pp. 212–219, 2018.

[27] T. Bui-Thanh, M. Damodaran, and K. Willcox, *Aerodynamic data reconstruction and inverse design using proper orthogonal decomposition*, AIAA Journal, vol. 42, pp. 1505-1516, 2004.

[28] X. Zou, M. Conti, P. Dìez, and F. Auricchio, *A non-intrusive proper generalized decomposition scheme with application in biomechanics*, International Journal for Numerical Methods in Engineering, vol. 113, 2017.

[29] S. Volkwein, *Proper orthogonal decomposition: Theory and reduced order modelling*, Lecture Notes, University of Konstanz, 01 2012.

[30] G. Stabile and G. Rozza, *Finite volume pod-galerkin stabilised reduced order methods for the parametrised incompressible navier–stokes equations*, Computers & Fluids, vol. 173, pp. 273–284, 2018.

[31] F. Ballarin, A. Manzoni, G. Rozza, and S. Salsa, *Shape optimization by free-form deformation: Existence results and numerical solution for Stokes flows*, Journal of Scientific Computing, vol. 60, pp. 537–563, 3 2014.

[32] A. Quarteroni and G. Rozza, *Numerical solution of parametrized Navier–Stokes equations by reduced basis methods*, Numerical Methods for Partial Differential Equations, vol. 23, pp. 923-948, 4, 2007.

[33] A. Quaini, S. Canic, D. Paniaqua, *Numerical characterization of hemodynamics conditions near aortic valve after implantation of Left Ventricular Assist Device*, Mathematical Biosciences and Engineering, vol. 8, pp. 785-806, 3 2011.

[34] A. Aliseda, V. K. Chivukula, P. Mcgah, A. R. Prisco, J. A. Beckman, G. J. M. Garcia, N. A. Mokadam, and C. Mahr, *LVAD outflow graft angle and thrombosis risk*, ASAIO Journal, vol. 63, pp. 14-23, 1 2017.

[35] B. Barrick, A. Smeltz, A. Ganesh, H. Arora, and P. Kumar, *Aortic valve thrombus in a patient with an extracorporeal left305 ventricular assist device: The dilemma of management*, Journal of Cardiothoracic and Vascular Anesthesia, vol. 30, 2015.

[36] Y. Bazilevs, J. Gohean, T. Hughes, R. Moser, and Y. Zhang, *Patient-specific isogeometric fluid–structure interaction analysis of thoracic aortic blood flow due to implantation of the jarvik 2000 left ventricular assist device*, Computer Methods in Applied Mechanics and Engineering, vol. 198, pp. 3534–3550, 45-46 2009.

[37] R. Mazzitelli, F. Boyle, E. Murphy, A. Renzulli, and G. Fragomeni, *Numerical prediction of the effect of aortic left ventricular assist device outflow-graft anastomosis location*, Biocybernetics and Biomedical Engineering, vol. 36, pp. 327–343, 2 2016.

[38] A. F. Osorio, R. Osorio, A. Ceballos, R. Tran, W. Clark, E. A. Divo, I. R. Argueta-Morales, A. J. Kassab, and W. M. DeCampli, *Computational fluid dynamics analysis of surgical adjustment of left ventricular assist device*

implantation to minimise stroke risk, Computer Methods in Biomechanics and Biomedical Engineering, vol. 16, pp. 622–638, 6 2013.

[39] K. May-Newman, B. Hillen, C. Sironda, and W. Dembitsky, *Effect of LVAD outflow conduit insertion angle on flow through the native aorta*, Journal of medical engineering & technology, vol. 28, pp. 105-109, 2004.

[40] J. Bonnemain, A. C. I. Malossi, M. Lesinigo, S. Deparis, A. Quarteroni, and L. Segesser, *Numerical simulation of left ventricular assist device implantations: Comparing the ascending and the descending aorta cannulations*, Medical engineering & physics, vol. 35, pp. 1465–1475, 2013.

[41] T. Zbigniew, D. Obidowski, and K. Jozwik, *Numerical analysis of the VAD outflow cannula positioning on the blood flow in the patient–specific brain supplying arteries*, Mechanics and Mechanical Engineering, vol. 22, pp. 619–635, 2018.

[42] Z. Demirozu and O. Frazier, *Aortic valve noncoronary cusp thrombosis after implantation of a nonpulsatile, continuous-flow pump*, Texas Heart Institute of St. Luke's Episcopal Hospital, Texas Children's Hospital, vol. 39, pp. 618-620, 2012.

[43] J. Crestanello, D. Orsinelli, M. Firstenberg, and C. Sai-Sudhakar, *Aortic valve thrombosis after implantation of temporary left327 ventricular assist device*, Interactive cardiovascular and thoracic surgery, vol. 8, pp. 661-662, 2009.

[44] J. Fried, J. Han, Y. Naka, U. Jorde, and N. Uriel, *Myocardial infarction after left ventricular assist device implantation: Clinical course, role of aortic root thrombus, and outcomes*, The Journal of heart and lung transplantation: the official publication of the International Society for Heart Transplantation, vol. 33, pp. 112-115, 2014.

[45] Columbia Heart Surgery. Avaiable at: **https://columbiasurgery.org/conditions-and-treatments/ventricular-assist-devices**.

[46] A. E. Eshelman, S. Mason, H. Nemeh and C. Williams, *LVAD destination therapy: applying what we know about psychiatric evaluation and management from cardiac failure and transplant*, Heart Failure Reviews, vol. 14, 21 2009.

[47] J. K. Kirklin, D. C. Naftel, F. D. Pagani, R. L. Kormos, L. Stevenson, M. Miller, J. B. Young, *Long-term mechanical circulatory support (destination therapy): On track to compete with heart transplantation?*, The Journal of Thoracic and Cardiovascular Surgery, vol. 144, pp. 584-603, 3 2012.

[48] C. Nabors, S. J. Peterson and W. H. Frishman, *The Modern Hospital*, Springer Publishing, 2019.

[49] P. B. Bochev, M. D. Gunzburger, J. N. Shadid, *Stability of the SUPG finite element method for transient advection–diffusion problems*, Computer Methods in Applied Mechanics and Engineering, vol. 193, pp. 2301-2323, 2004.

[50] T. Corporation, *Heartmate 3 left ventricular assist system: Instructions for use*, 2017.

[51] Y. Shi, P. Lawford, and D. Hose, *Numerical modeling of hemodynamics with pulsatile impeller pump support*, Annals of biomedical engineering, vol. 38, pp. 2621–2634, 2010.

[52] N. Westerhof, J. W. Lankhaar, and B. Westerhof, *The arterial windkessel*, Medical & biological engineering & computing, vol. 47, pp. 131–41, 2008.

[53] W. Laskey, H. Parker, V. Ferrari, W. Kussmaul, and A. Noordergraaf, *Estimation of total systemic arterial compliance in humans*, Journal of Applied Physiology. vol. 69, pp. 112–119, 1990.

[54] C. Bulpitt, J. Cameron, C. Rajkumar, S. Armstrong, M. Connor, J. Joshi, D. Lyons, O. Moioli, and P. Nihoyannopoulos, *The effect of age on vascular compliance in man: Which are the appropriate measures?*, Journal of human hypertension, vol. 13, pp. 753-758, 1999.

[55] F. Moukalled, L. Mangani, and M. Darwish, *The Finite Volume Method in Computational Fluid Dynamics: An Advanced Introduction with OpenFOAM and Matlab.*, Springer Publishing Company, Incorporated, 2015.

[56] J. H. Ferziger and M. Peric, *Computational Methods for Fluid Dynamics.* Berlin: Springer, 1999.

[57] H. G. Weller, G. Tabor, H. Jasak, and C. Fureby, *A tensorial approach to computational continuum mechanics using objectoriented techniques*, Computers in physics, vol. 12, pp. 620–631, 6 1998.

[58] H. Jasak, *Error analysis and estimation for the finite volume method with applications to fluid flows*, Ph.D. thesis, Imperial College, University of London, 1996.

[59] G. V. Patankar and D. B. Spalding, *A calculation procedure for heat, mass and momentum transfer in three-dimensional parabolic flows*, International Journal of Heat and Mass Transfer, vol. 15, pp. 1787–1803, 10 1972.

[60] R. I. Issa, *Solution of the implicitly discretised fluid flow equations by operator-splitting*, Journal of Computational Physics, vol. 62, pp. 40-65, 1 1986.

[61] F. Moukalled, L. Mangani, and M. Darwish, *The finite volume method in computational fluid dynamics: An advanced introduction with openfoam and matlab*, Springer Publishing Company, Incorporated, 2015.

[62] A. Quarteroni and G. Rozza, *Numerical solution of parametrized Navier–Stokes equations by reduced basis methods*, Numerical Methods for Partial Differential Equations, vol. 23, pp. 923–948, 4 2007.

[63] S. Makridakis, *Accuracy measures: theoretical and practical concerns*, International Journal of Forecasting, vol. 9, pp. 527-529, 4 1993.

[64] E. Farag, P. Ooij, R. Planken, K. Dukker, F. Heer, B. Bouma,

D. Robbers-Visser, M. Groenink, A. Nederveen, B. Mol, J. Kluin, and S. Boekholdt, *Aortic valve stenosis and aortic diameters determine the extent of increased wall shear stress in bicuspid aortic valve disease: AS and aortic diameters determine WSS in BAV*, Journal of Magnetic Resonance Imaging, vol. 48, 2018.

[65] P. Ooij, M. Markl, J. Collins, J. Carr, C. Rigsby, R. Bonow, S. Malaisrie, P. McCarthy, P. Fedak, and A. Barker, *Aortic valve stenosis alters expression of regional aortic wall shear stress: New insights from a 4-dimensional flow magnetic resonance imaging study of 571 subjects*, Journal of the American Heart Association, vol.6, 2017, e005959.

[66] R. Lorenz, J. Bock, A. Barker, F. von Knobelsdorff, W. Wallis, J. Korvink, M. Bissell, J. Schulz-Menger, and M. Markl, *4D flow magnetic resonance imaging in bicuspid aortic valve disease demonstrates altered distribution of aortic blood flow helicity*, Magnetic resonance in medicine, vol. 71, 2014.

[67] A. Aliseda, V. K. Chivukula, P. Mcgah, A. R. Prisco, J. A. Beckman, G. J. M. Garcia, N. A. Mokadam, and C. Mahr, *LVAD outflow graft angle and thrombosis risk*, ASAIO Journal, vol. 63, pp. 14–23, 1, 2017.

[68] M. V. Caruso, V. Gramigna, M. Rossi, G. F. Serraino, A. Renzulli, and G. Fragomeni, *A computational fluid dynamics comparison between different outflow graft anastomosis locations of left ventricular assist device (LVAD) in a patient-specific aortic model*, International Journal for Numerical Methods in Biomedical Engineering, vol. 31, 2 2015, e02700.

[69] Q. Zhang, B. Gao, and Y. Chang, *Helical flow component of left ventricular assist devices (LVADs) outflow improves aortic hemodynamic states*, Medical Science Monitor, vol. 24, pp.869-879, 2018.

[70] C. Karmonik, S. Partovi, M. Loebe, B. Schmack, A. Ghodsizad, M. R. Robbin, G. P. Noon, K. Kallenbach, M. Karck, M. G. Davies, A. B. Lumsden, and A. Ruhparwar, *Influence of LVAD cannula outflow tract location on hemodynamics in the ascending aorta: A patient-specific computational fluid dynamics approach*, ASAIO Journal, vol. 58, pp. 562–567, 6 2012.

[71] C. Karmonik, S. Partovi, M. Loebe, B. Schmack, A. Weymann, A. B. Lumsden, M. Karck, and A. Ruhparwar, *Computational fluid dynamics in patients with continuous-flow left ventricular assist device support show hemodynamic alterations in the ascending aorta*, The Journal of Thoraci and Cardiovascular Surgery, vol. 147, pp. 1326-1333, 4 2014.

[72] C. Karmonik, S. Partovi, B. Schmack, A. Weymann, M. Loebe, G. P. Noon, P. Piontek, M. Karck, A. B. Lumsden, and A. Ruhparwar, *Comparison of hemodynamics in the ascending aorta between pulsatile and continuous flow left ventricular assist devices using computational fluid dynamics based on computed tomography images*, Artificial Organs, vol. 38, pp. 142–148, 2 2014.

[73] K. May-Newman, B. Hillen, and W. Dembitsky, *Effect of left ventricular assist device outflow conduit anastomosis location on flow patterns in the native aorta*, ASAIO journal, vol. 52, pp. 132–139, 2006.

[74] G. Inci and E. Sorguven, *Effect of LVAD outlet graft anastomosis angle on the aortic valve, wall, and flow*, ASAIO Journal, vol. 58, pp. 373-381, 4 2012.

[75] A. Brown, Y. Shi, A. Arndt, J. Muller, P. Lawford, and D. Hose, *Importance of realistic lvad profoles for assisted aortic simulations: Evaluation of optimal outflow anastomosis locations*, Computer Methods in Biomechanics and Biomedical Engineering, vol. 15, pp. 669–680, 2011.

[76] Q. Zhang, B. Gao, and Y. Chang, *Helical flow component of left ventricular assist devices (LVADs) outflow improves aortic hemodynamic states*, Medical Science Monitor, vol. 24, pp. 869-879, 2018.

[77] J. Dolan, H. Meng, S. Singh, R. Paluch, and J. Kolega, *High fluid shear stress and spatial shear stress gradients affect endothelial proliferation, survival, and alignment*, Annals of biomedical engineering, vol. 39. pp. 1620-31, 2011.

[78] A. Malek, *Hemodynamic shear stress and its role in atherosclerosis*, JAMA, vol. 282, pp. 2035, 1999.

[79] M. V. Caruso, V. Gramigna, M. Rossi, G. F. Serraino, A. Renzulli, and G. Fragomeni, *A computational fluid dynamics comparison between different outflow graft anastomosis locations of left ventricular assist device (LVAD) in a patient-specific aortic model*, International Journal for Numerical Methods in Biomedical Engineering, vol. 31, e02700, 2 2015.

[80] J. Bonnemain, S. Deparis, and A. Quarteroni, *Connecting ventricular assist devices to the aorta: A numerical model*, Springer Milan, pp. 211–224, 2012.

[81] A. Aliseda, V. K. Chivukula, P. Mcgah, A. R. Prisco, J. A. Beckman, G. J. M. Garcia, N. A. Mokadam, and C. Mahr, *LVAD outflow graft angle and thrombosis risk*, ASAIO Journal, vol. 63, pp. 14–23, 1 2017.

[82] J. S. Hesthaven, G. Rozza, and B. Stamm, *Certified Reduced Basis Methods for Parametrized Partial Differential Equations.* Springer Briefs in Mathematics, Switzerland: Springer, 1 2015.

[83] Benner, P., Ohlberger, M., Pater, A., Rozza, G., Urban,K, *Model Reduction of Parametrized Systems.*,MS&A series, vol. 1, Springer, 2017.

[84] P. Benner, W. Schilders, S. Grivet-Talocia, A. Quarteroni, G. Rozza, and L. M. Silveira, *Model order reduction, De Gruyter, Berlin, Boston, 2020.* URL **://www.degruyter.com/view/title/523453.**

[85] S. Buoso, A. Manzoni, H. Alkadhi, A. Plass, A. Quarteroni, and V. Kurtcuoglu, *Reduced-order modeling of blood flow for noninvasive functional evaluation of coronary artery disease.* Biomech Model Mechanobiol vol. 18, pp. 1867–1881, 2019.